Optofluidic Lasers and Their Bio-sensing Applications

by

Wonsuk Lee

A dissertation submitted in partial fulfillment
of the requirements for the degree of
Doctor of Philosophy
(Electrical Engineering)
in The University of Michigan
2013

Doctoral Committee:

Associate Professor Xudong Fan, Co-chair
Professor L. Jay Guo, Co-chair
Professor David T. Burke
Associate Professor Pei-Cheng Ku

TABLE OF CONTENTS

LIST OF FIGURES

Figure

LIST OF TABLES

Table

ABSTRACT

Optofluidic Lasers and Their Bio-sensing Applications

by

Wonsuk Lee

Novel optofluidic ring resonator (OFRR) lasers resolving problems of existing lasers have been demonstrated and DNA melting analysis taking advantages of the OFRR laser is suggested.

The OFRR laser fabricated on a polymer chip utilizes two optically coupled ring resonators in different sizes in order to address an intrinsic multi-mode emission of the ring resonator laser. A single-mode emission is obtained by Vernier effect and the wavelength is tunable by modifying the refractive index of the gain medium.

A quasi-droplet OFRR laser is developed based on a micro-bubble filled with liquid gain medium. Due to the sub-micron wall thickness, the micro-bubble mimics a droplet in air that has 3-dimensional optical confinement, extremely high Q-factor and versatility of handling liquids of different refractive index. The laser using Rhodamine 6G in methanol has low lasing thresholds and dye concentration. Furthermore, it enables

repetitive interrogation and easy directional laser emission out-coupling without evaporation or size/shape variations.

Microdroplets in carrier fluid are delivered to the capillary OFRR downstream and laser emission is obtained. The laser can conveniently be coupled into an optical fiber and lasing threshold 6 times lower than the state-of-art is achieved. An efficient FRET lasing is also demonstrated making the OFRR droplet laser an attractive platform of bio/chemical sensing with small sample volume.

In last, a highly specific intracavity DNA melting analysis scheme utilizing the optofluidic laser is proposed. The laser optically amplifies the small yet intrinsic thermal dynamic difference between the target and the single-base-mismatched DNA, resulting in a differential signal that is orders of magnitude greater than with fluorescence-based methods. In particular, the existence of a phase transition between the stimulated laser emission and fluorescence enables accurate determination of the DNA transition temperature difference. Furthermore, the high differential signal in the intracavity detection allows for scanning of the laser excitation at a fixed temperature to distinguish two DNA sequences, which provides another means for rapid DNA analysis. The intracavity DNA detection leads to novel optofluidic devices that enable rapid and simple analysis of DNAs with long sequences.

Chapter I

Introduction

1.1 Optofluidic laser

Optofluidics is a field developing optical systems that are synthesized with fluids, which suggests a synergic combination of optics and micro/nanofluidics.(1-4) Liquids have unique properties that can be utilized to design multi-functional optical devices and these properties cannot be found in solid-state equivalents. For example, researchers can find molecularly smooth interfaces in between two immiscible liquids. These smooth surfaces can lead to an optical resonator and/or a laser cavity with extremely high Q-factor. In contrast, two miscible fluids can create optically gradient interfaces by diffusion. More than the interfaces, optofluidic system can change its own optical properties by simply replacing the liquid medium within a device from one fluid to another. Moreover, since the optofluidic system is based on already mature microfluidics technology, any microfluidic fabrication methods and processes can, in principle, be adapted to develop optofluidic devices. Micro/nanofluidics is also a burgeoning field with important applications in biotechnology and analytical chemistry.(5) Most of biochemical reactions should be reproduced in water, thus the optofluidic system based on micro/nanofluidics has intrinsic advantages in biological sensing applications.

Optofluidic dye laser is a class of dye laser system, which utilizes fluid, usually an organic laser dye dissolved liquid, as a laser gain medium.(6-9) It has been intensively

investigated because of their potential of integration in micrototal analysis systems (μTAS), compatibility with microfluidic components, and wavelength tunability.(1, 3, 4, 6) They have been realized with various types of optical cavities explored, such as distributed-feedback (DFB) gratings (9-16) and Fabry-Perot resonators (8, 15, 17-19), as shown in Fig. 1.1. Such laser devices, however, have relatively high lasing thresholds due to low Q-factors of their microcavities. Since low energy operation is essential for bio-compatible devices, optofluidic laser devices with conventional optical cavities have limited potential particularly for bio-molecular sensing applications.

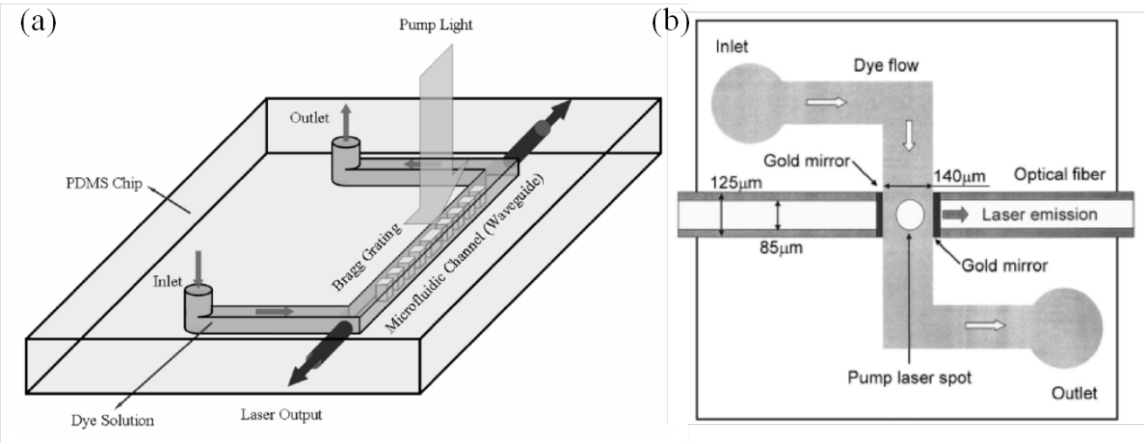

Figure 1.1 (a) Optofluidic laser based on distributed feedback microcavity fabricated on polymer substrate. (b) Fabry-Perot cavity laser with two optical fibers and microfluidics channel. Reprinted with permission from Refs. (10, 17).

1.2 Optofluidic ring resonator

Optical ring resonator is a waveguide with a closed loop, usually ring-shaped, which supports the circulating resonant waveguide mode or the whispering gallery mode (WGM) by total internal reflection of light at the curved boundary. The resonant wavelength, λ, is given by (20, 21):

$$\lambda = \frac{2\pi r n_{eff}}{m} \tag{1.1}$$

where r is the resonant radius, neff is the effective refractive index experienced by the optical resonant mode and m is an integer.

The optical ring resonator can be adapted to the development of the optofluidic laser and/or sensors. The resonant light circulates along the ring resonator and has evanescent field into the surrounding medium, thus interacts repetitively with the liquid, gas or analytes near the resonator surface, as shown in Fig. 1.2.(22-30) In the ring resonator based optofluidic lasers, the lasing properties are also determined by light-medium interaction, in which case, the medium becomes dye molecules or other gain materials.(7, 9, 31, 32)

The optofluidic ring resonator (OFRR) lasers have several advantages over conventional laser cavities, mainly due to their extremely high Q-factors. The optical cavity with high Q-factor leads to the low lasing threshold while low energy operation is particularly important for biological applications. Furthermore, the ring resonator devices take advantage of small footprint, enabling large scale integration to the lab-on-a-chip systems.(33-41)

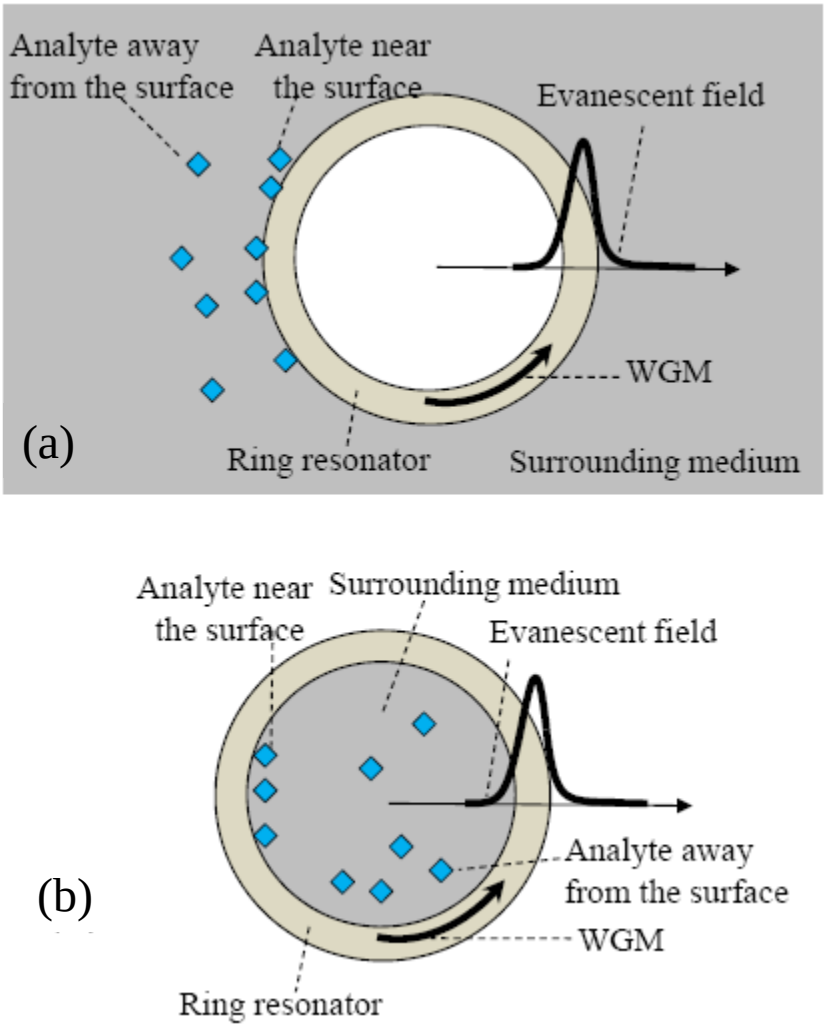

Figure 1.2 The resonant light circulating along the ring resonator circumference has evanescent field in the surrounding medium outside (a) or inside (b) the ring resonator. Interaction with the analyte in the surrounding medium leads to optical gain for optofluidic laser applications. Reprinted from Ref. (22) with permission.

1.3 DNA detection

Analyzing or resolving small thermal dynamics of two DNA strands is very important in many biomedical and biological applications, such as Single-nucleotide polymorphism (SNP) and/or target DNA sequence detection.(42, 43) In order to explore a detailed knowledge on the DNA sequence, many genotyping methods have been proposed.(44-49) Most hybridization-based methods, such as dynamic allele-specific hybridization genotyping, molecular beacons, and DNA microarrays utilize a fluorescence signal from the dye molecules labeled to the DNA sequences.(50-55) While the labeling process requires complexity and cost to the genotyping, the discrimination ratio between the fluorescent signal from the target and the SNP is near unity, especially for the longer DNA sequences. Other post-amplification methods are based on the physical properties of DNA, mostly difference in melting temperature between the target and the mismatch.(50, 56) High resolution melting (HRM) analysis is the simplest fluorescence-based method followed by polymerase chain reaction (PCR).(45, 47, 57-61) A fluorimeter monitors the denaturation of the double-stranded DNA (dsDNA) by the fluorescent signal from a double-stranded specific dye, the saturation dye in other words. However, this process takes long time scanning the dynamic temperature range and plenty of heating on the biological samples is undesirable for most in vivo DNA detecting. Moreover, since the difference in the melting temperature and the fluorescence of the target and SNP is small, this requires highly optimized conditions to obtain the best possible results. When the sensing mechanism is relying on lasing activity, several orders of magnitude higher discrimination ratio can be achieved due to the nature of laser, thus can obtain higher sensitivity.(62)

1.4 Organization

In this thesis, novel optofluidic ring resonator laser schemes, which overcome drawbacks of existing optofluidic lasers, are suggested. Furthermore, DNA sequence analysis utilizing the OFRR laser is demonstrated.

From Chapter 2 to 4, development of different types of the OFRR laser are presented. In Chapter 2, a single-mode lasing from the PDMS-based OFRR laser is demonstrated. The novel OFRR laser overcomes an intrinsic drawback of the OFRR laser, which is a multi-wavelength emission, and demonstrates a wavelength tunablility at the same time. In Chapter 3, a quasi-droplet laser mimicking a natural droplet laser using micro-bubble fabrication technique is illustrated. Chapter 4 focuses on a micro-capillary based OFRR laser associated with a micro-droplet generating system. Chapter 5 proposes a novel DNA melting analysis utilizing the OFRR laser. Chapter 6 covers a brief summary and outlook towards future work directions.

Chapter II

Tunable Single Mode Lasing from an On-chip Optofluidic Ring Resonator Laser

Single mode lasing from the polydimethylsiloxane based on-chip coupled optofluidic ring resonator OFRR with the lasing threshold of a few $\mu J/mm^2$ is demonstrated using the Vernier effect. The single mode operation is highly stable even at high pump energy densities. The effect of the OFRR size and coupling strength on the single mode emission is investigated, showing that the excessive coupling results in incomplete side mode suppression. Tuning of the lasing wavelength is achieved by modifying the dye solution.

2.1 Motivation

Optofluidic dye lasers have been intensively investigated because of their small footprint, potential of integration in lab-on-a-chip devices, and wavelength tunability. As compared to other types of optical cavities explored for optofluidic lasers, such as Fabry-Perot resonators (8, 15, 17-19), distributed-feedback (DFB) gratings (9-16), optofluidic ring resonators (OFRRs) that support the circulating resonant mode called the whispering gallery mode (WGM) take advantage of compact size and relatively high Q-factors, both of which are key to achieving large scale integration and low lasing thresholds. The

OFRR lasers have previously been implemented in the form of discrete ring cavity,(63) microdroplets (64, 65) microknots (66), microcylinder (67-69), and microcapillaries (7) as shown in Fig. 2.1.

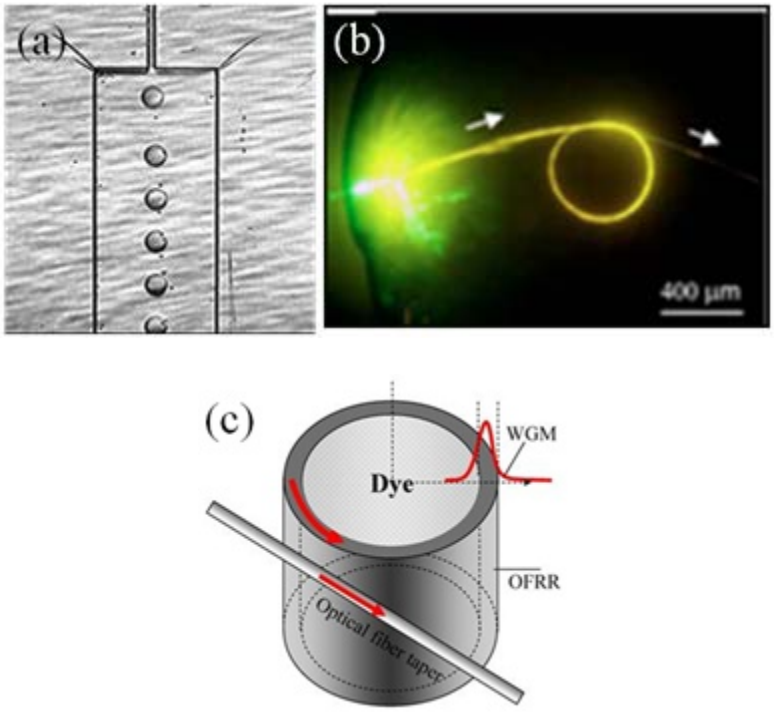

Figure 2.1 OFRR lasers with (a) microdroplets, (b) microknot and (c) microcapillary optical cavities. Reprinted with the permission from Ref. (7, 65, 66).

Very recently, on-chip polydimethylsiloxane (PDMS) based OFRRs were also demonstrated (70, 71) as in Fig. 2.2. Since the entire PDMS device can be fabricated by simple replica molding processes, cost-effective mass production of the OFRR lasers becomes possible. The OFRR lasers have very large possibilities as not only the light source of the μTAS, but also as a bio/chemical detection platform by themselves.

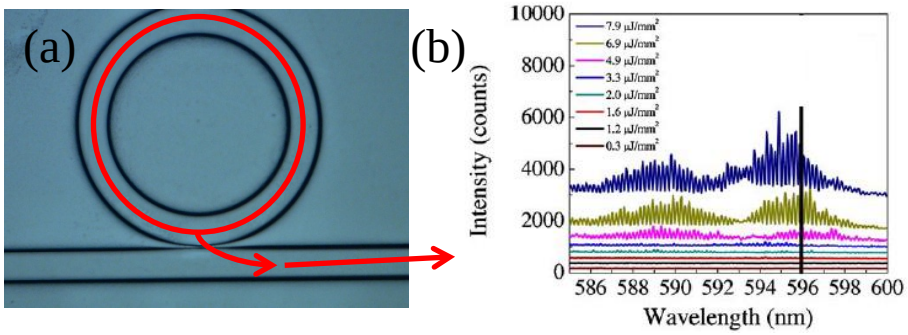

Figure 2.2 (a) OFRR laser fabricated on PDMS substrate. Red arrows indicates propagation of the resonant and waveguided light. (b) Lasing spectra from the laser device in different pump energy densities. Reprinted with the permission from Ref. (70).

However, the OFRR laser intrinsically has multi-mode lasing emission as shown in Fig. 2.2 (b), due to its narrow free spectral range (FSR), which is a major drawback as compared to the DFB based optofluidic laser that is capable of single mode operation. As explained in Chapter 1, the light with the wavelength satisfying Eq. (1.1) is supported by the resonance. By simple math, the FSR can be obtained by:

$$\Delta\lambda = \lambda_0^2 / 2\pi n_{eff} D \tag{2.1}$$

where λ_0 is central wavelength, n_{eff} is the effective refractive index and D is a diameter of the ring. Rhodamine 6G (R6G) is an organic dye widely used for optofluidic lasers and has wavelength of laser emission around 600 nm and the gain profile lies within 10 to 20 nm range.(6) When the ring diameter is 50 microns, which is a typical value for high Q-factor microring, the FSR becomes less than 0.8 nm. In that case, approximately 20 to 30 possible modes exist within the gain profile range, and most of those modes will not be suppressed. One of the methods to suppress the side modes is to utilize the Vernier effect, in which two ring resonators of different FSRs are coupled to each other. While the single mode laser emission has been achieved in on-chip solid coupled ring resonators (32, 72,

73), on-chip OFRR single mode lasers and their lasing characteristics have not been studied.

In this Chapter, we develop and characterize the single mode laser using a PDMS based coupled OFRR. The effect of the OFRR size and coupling strength on the single mode emission is investigated and the tuning of the lasing wavelength over both small and large spectral range is demonstrated. We show that stable single mode laser emission can be obtained with the lasing threshold on the order of a few $\mu J/mm^2$.

2.2 Vernier effect

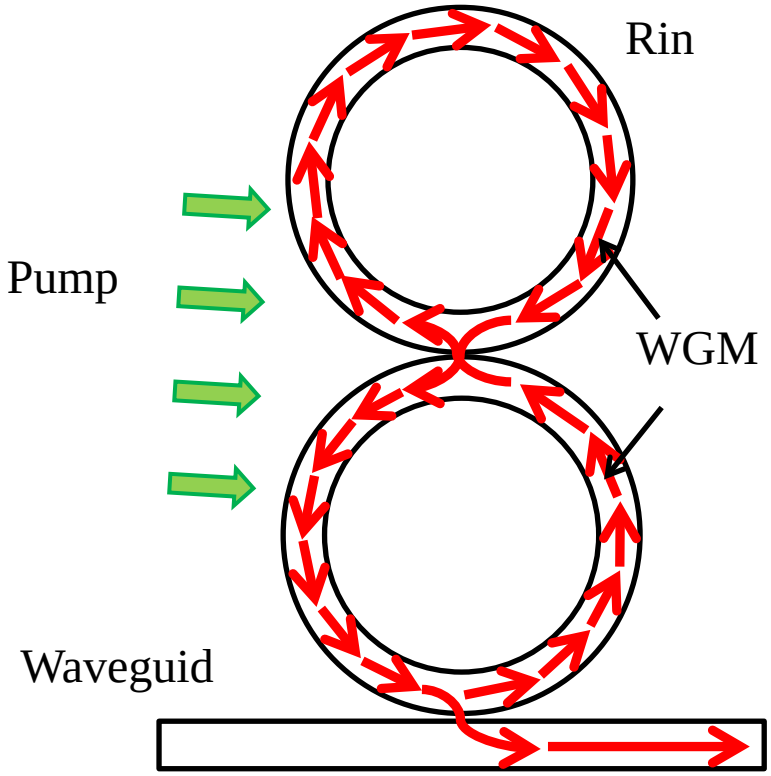

Figure 2.3 Schematic of a coupled OFRR laser. The red arrows inside the ring resonator and the waveguide show the light propagation.

Our approach to suppress the side modes relies on Vernier effect, in which two ring resonators of different FSRs are coupled to each other. Fig. 2.3 shows a schematic of the coupled OFRR laser system consisting of two size mismatched ring resonators and a liquid-filled waveguide. When two different ring resonators are optically coupled, light with the wavelength that can be supported by both of two rings will be resonant. In that case, the FSR of the coupled ring resonators can be obtained by Vernier equation:

$$\Delta\lambda=\lambda^2/\pi n_{eff}(D_1-D_2) \qquad (2.2)$$

where λ is the lasing wavelength, n_{eff} is the effective RI and the diameters of the two rings are D_1 and D_2. As long as the difference between the size of the two rings remain

small, the FSR can be maintained large enough to suppress the side modes. For example, the FSR becomes around 8 nm for the OFRR laser with R6G when the size difference is 10 μm. Since the width of the gain profile of R6G is 10 to 20 nm, a single mode operation becomes possible for such cases. A significant advantage of this approach is that we can successfully suppress side modes without decreasing the size of the ring resonator, since the Q-factor of ring resonator is directly affected by the size.

2.3 Fabrication and experiments

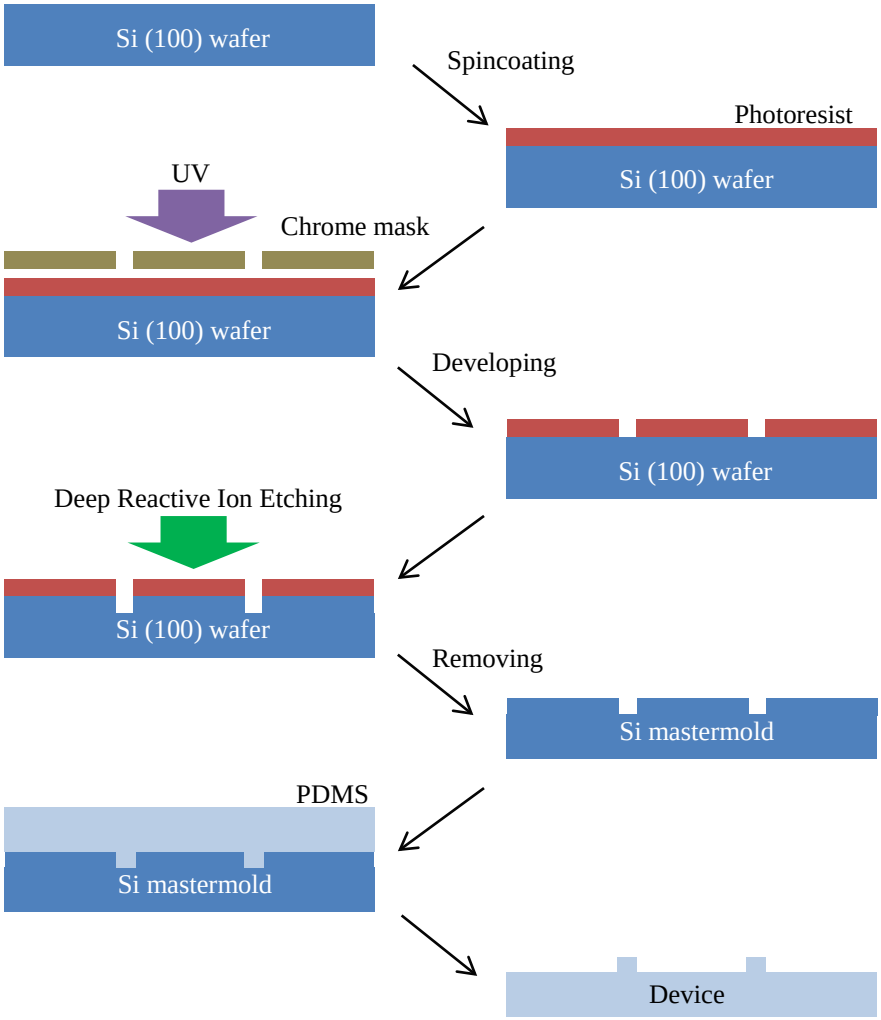

Figure 2.4 Flow chart of device fabrication.

The device is produced in PDMS by replica molding process as in Fig. 2.4.(74-76) The master mold is first fabricated on a silicon wafer by photolithography and reactive ion etching. The silicon wafer is first spincoated with a photoresist (PR) SPR 220 at the thickness of 3 μm. The wafer is then exposed with UV light under a chrome mask consists of the ring resonator and the waveguide patterns. After developing the PR, the

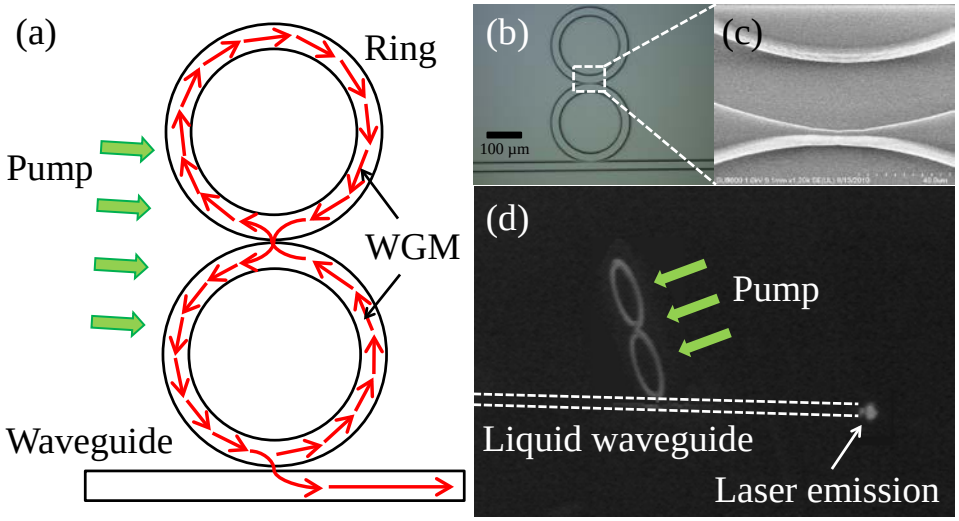

Figure 2.5 (a) Schematic of a coupled OFRR laser. The arrows inside the ring resonator show the light propagation direction. (b) Microscopic image of the two ring resonators and the waveguide formed on the PDMS substrate. The diameter of the upper (lower) ring is 290 (300) μm. The gap between the lower ring and the waveguide and between the two rings is 2 μm and 1 μm, respectively. The two rings are filled with dye dissolved in TEG, whereas the waveguide is filled with TEG alone. (c) SEM image of the 1 μm gap between the two rings. (d) Photograph of the coupled OFRR during laser operation. The laser emission is coupled into the liquid waveguide and collected at its distal end. Dashed lines show the waveguide position.

wafer is etched by the deep reactive ion etching (DRIE) for the intended depth of 15 μm.(77) Remaining PR is removed by PR-remover. The wafer is then vacuum-coated with trichlorosilane and subsequently coated with uncured PDMS. Finally, the PDMS is cured at room temperature for 48 hours before it is peeled off from the wafer and treated with O2 plasma. The resulting circular and straight liquid channels are shown in Fig. 2.5(b) and (c), which are 40 μm in width and 10 μm in depth. The two ring resonators (the lower ring and the straight waveguide) are separated by a 1 μm (2 μm) PDMS gap, respectively. Consequently, they are optically coupled but physically disconnected. During the experiment, dye dissolved in tetraethylene glycol (TEG) is introduced into the two OFRRs, whereas the waveguide is filled with TEG alone. Since the refractive index

(RI) of TEG (1.456) is larger than that of PDMS (1.42), light is confined in the gain medium and the liquid waveguide. The coupled OFRR is uniformly pumped by a 5 ns pulsed optical parametric oscillator at 532 nm, as illustrated in Fig. 2.5(a) and (d). The lasing emission is coupled into the liquid waveguide near the lower OFRR and detected at its distal end by a spectrometer (Horiba iHR550, resolution 0.06 nm).

2.4 Results and discussion

2.4.1 Lasing characteristics

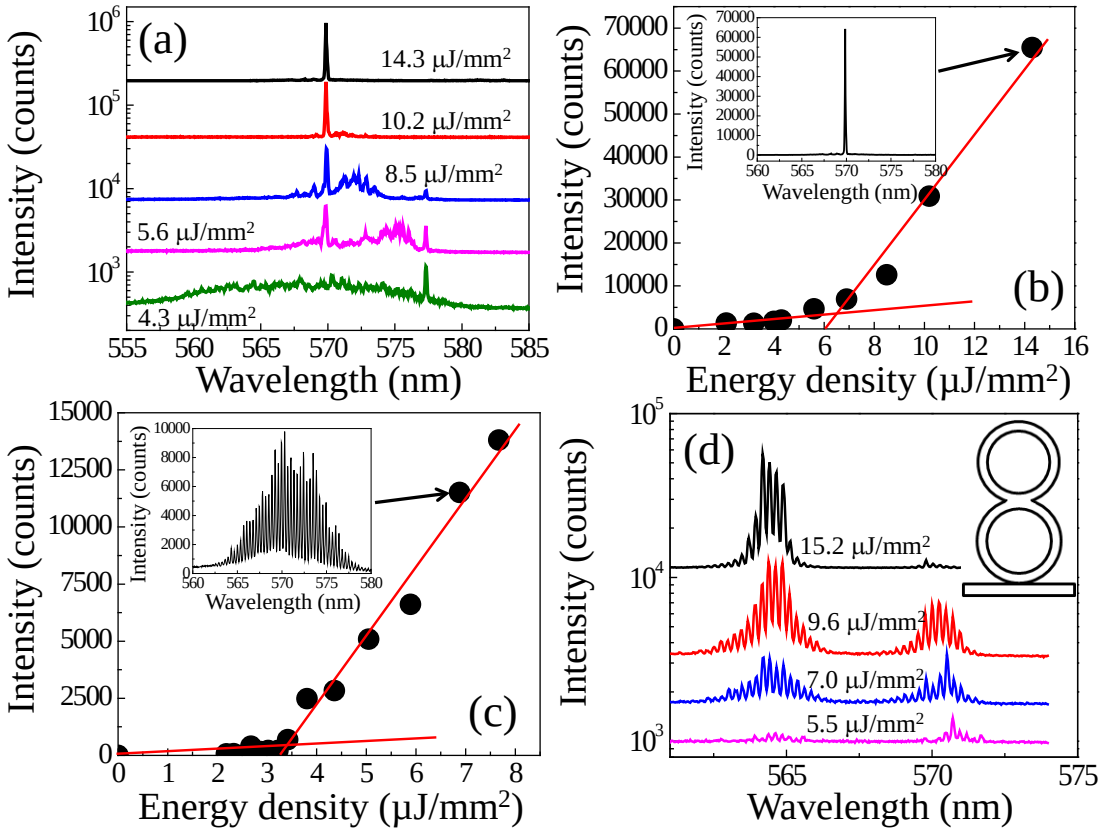

Figure 2.6 (a) Lasing spectra of the coupled OFRR laser described in Fig. 2.1(b) at various pump energy densities. Curves are vertically shifted for clarity. (b) Intensity of the laser emission at 569.9 nm as a function of the pump energy density. The lasing threshold is approximately 6 μJ/mm^2. Inset: lasing spectrum when the pump energy density is 14.3 μJ/mm^2. (c) Intensity of the laser emission from a single OFRR of 300 μm in diameter. The lasing threshold is 3.3 μJ/mm^2. Inset: lasing spectrum when the pump energy density is 6.9 μJ/mm^2. (d) Lasing spectra of the coupled OFRR laser when the two rings are in contact (contact region=19 μm). Curves are vertically shifted for clarity. 2 mM R6G is used in the experiments.

The lasing spectra of the coupled OFRR filled with 2 mM R6G at various pump energy densities are plotted in Fig. 2.6(a). At the lowest pump energy density, the single mode lasing emission occurs at 577.3 nm, whose lasing threshold is about 3 μJ/mm^2. As

the pump energy density increases, another strong mode emerges at 569.9 nm. These two modes result from the Vernier effect. In fact, the 7.4 nm spectral separation agrees well with the FSR calculated based on the Eq. 2.2, where λ (=575 nm), n_{eff} (=1.456), D_1 (=300 μm), and D_2 (=290 μm) are the lasing wavelength, the effective RI of the ring resonator, and the ring diameters, respectively. When the pump energy density continues to increase, the lasing at the Vernier mode at 577.3 nm diminishes whereas the strong and robust single mode lasing is sustained at another Vernier mode at 569.9 nm. This blue shift of the mode is attributed to the gain profile change under high pump intensities, as described earlier. The linewidth of this 569.9 nm mode is approximately 0.06 nm, limited by the spectrometer resolution. The corresponding lasing threshold curve is plotted in Fig. 2.6(b) with the lasing threshold of approximately 6 $\mu J/mm^2$. For comparison, the spectrum from a single OFRR laser (lower ring alone) is depicted in the inset of Fig. 2.6(c), showing the typical multi-mode lasing emission, which further confirms the Vernier effect on the single mode lasing operation. The lasing threshold in Fig. 2.6(c) is approximately 3.3 $\mu J/mm^2$.

2.4.2 Theoretical study

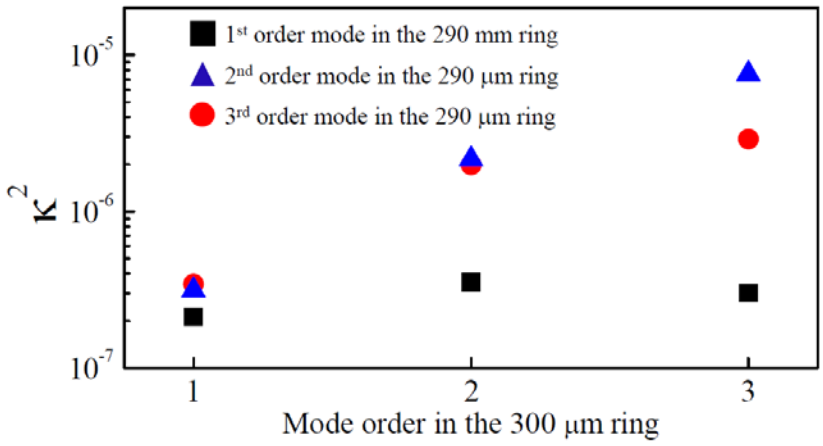

Figure 2.7 Coupling coefficient between the modes of the OFRRs described in Fig. 2.3.

Coupling between the two OFRRs plays an important role in obtaining the single mode lasing through the Vernier effect. Whereas inefficient coupling results in insufficient optical feedback provided by one ring to another, excessive coupling broadens the resonance linewidth (or decreases the Q-factor) of each OFRR. Both lead to degradation in side mode suppression. The coupling coefficient between the two OFRRs, κ, can be calculated by the coupled mode theory.(30, 78, 79) Fig. 2.7 presents the coupling coefficients among the first three orders of the modes in the coupled OFRR in Fig. 2.5 (b). The coupling related Q-factor, given by $n_{eff}\pi^2 D/\lambda\kappa^2$, should exceed 10^8. Similarly, we calculate the total coupling coefficient between the lower OFRR and the waveguide (*i.e.*, total fractional loss per round trip of the lower OFRR) to be on the order of 10^{-3}, corresponding to a Q ~7×10^6. Therefore, based on the Q-factor (~ 5000) experimentally observed in a single PDMS based OFRR in our previous studies,(70) we

infer that each ring in the current coupled OFRR system should have a similar Q-factor (~ 5000), which provides sufficient side mode suppression to achieve single mode operation, as shown in Fig. 2.5 (a).

In contrast, in Fig. 2.5 (d), the two rings are in contact with the width of the connected region of about 19 μm. In this case, the Q-factor of the OFRR is significantly spoiled due to the excessive coupling loss between the two rings. As a result, although the Vernier effect is still present (as evidenced by the clustered peaks separated by about 6 nm), it fails to completely suppress the side modes, leading to the emergence of well-spaced lasing modes that are modulated by the Vernier modes. The distance of the two adjacent modes is 0.235 nm, corresponding to the FSR of the 300 μm diameter OFRR. Although the coupled mode theory becomes invalid for us to calculate the coupling related Q-factor, it is estimated to be approximately 500 based on the Vernier mode profile in Fig. 2.5 (d). This Q-factor value is close to what was observed previously, in which the ring resonator has a similar contact region with a waveguide.

2.4.3 Size independence

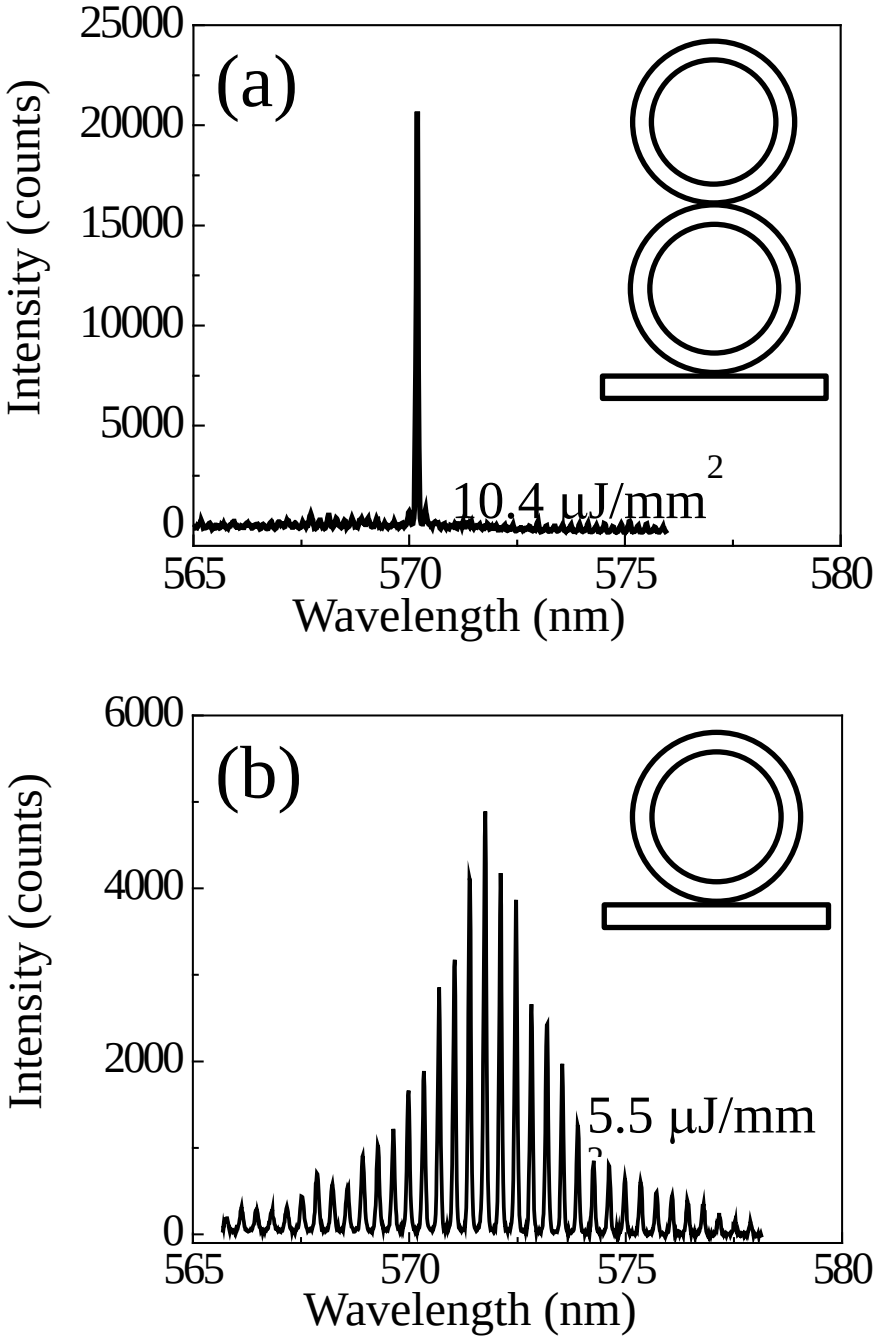

Figure 2.8 (a) Lasing spectrum from a coupled OFRR (190 μm and 200 μm in diameter, respectively). The gap between the lower ring and the waveguide and between the two rings is 2 μm and 1 μm, respectively. (b) Lasing spectrum from a single OFRR (200 μm in diameter). Gain medium is 2 mM R6G in TEG.

While the coupling between the two OFRRs affects the single mode operation of the OFRR laser, the size of the OFRRs does not deteriorate the properties of the lasing. As illustrated in Fig. 2.8(a), the single mode lasing can be achieved in the coupled OFRR with the respective diameter of 190 μm and 200 μm. According to the coupled mode theory, the coupling related loss is still negligible. As a result, the Q-factor of the OFRR (still a few thousand) is sufficient to suppress the side modes. Once again, in order to verify the Vernier effect, Fig. 2.8(b) shows the multi-mode lasing from the lower OFRR alone in the absence of the upper OFRR.

2.4.4 Wavelength tunability

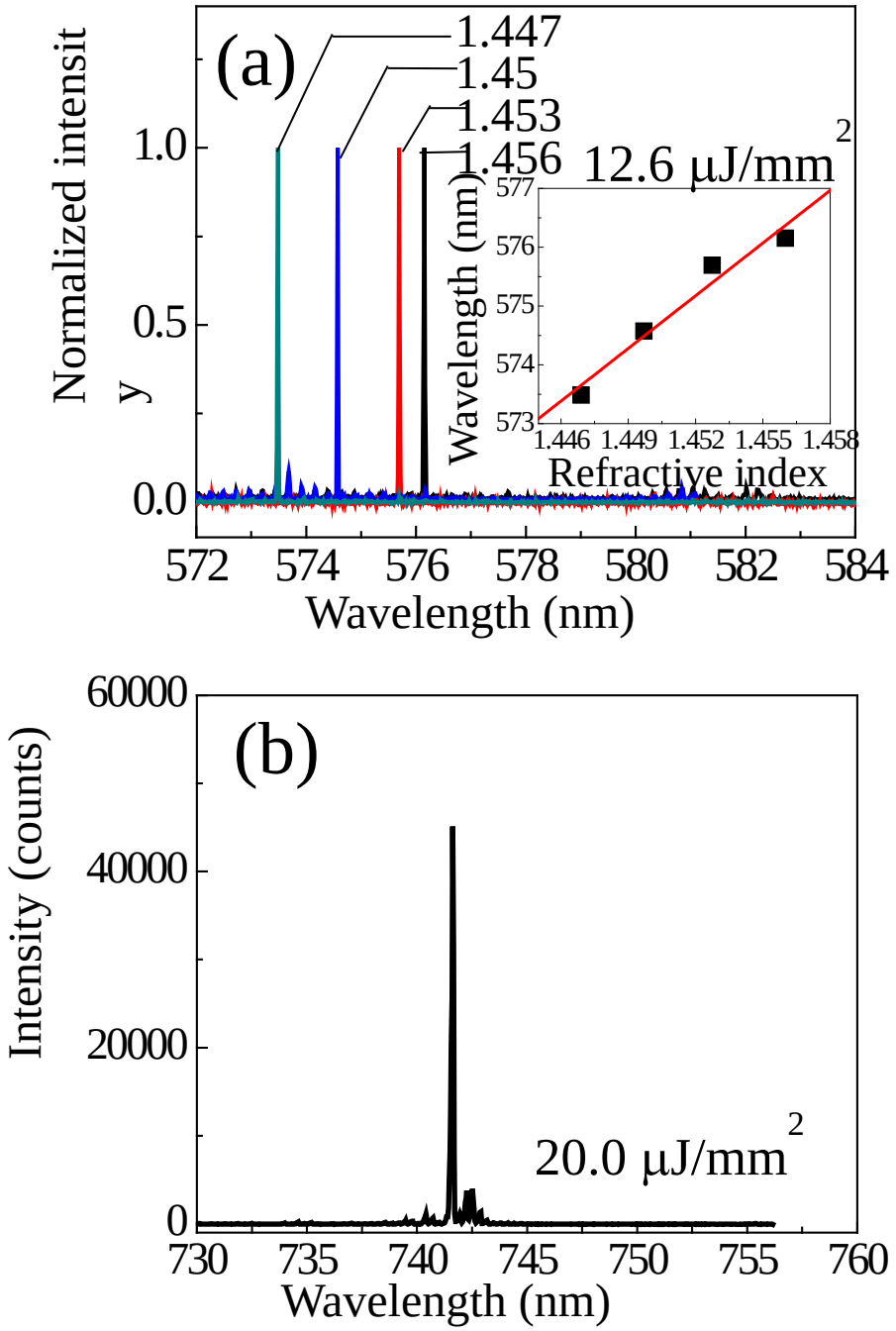

Figure 2.9 (a) Lasing spectra of the coupled OFRR laser described in Fig. 1(b) when the RI of 2 mM R6G solvent is varied by adding methanol to TEG. Inset: lasing wavelength as a function of solvent RI. (b) Lasing spectrum from 2 mM LDS 722 in TEG.

Since the lasing wavelength of the coupled OFRR laser is determined by the common resonant mode in the two OFRRs, the lasing wavelength can be tuned by changing the RI of the gain medium according to $\Delta\lambda/\lambda=\Delta n_{eff}/n_{eff}$, where $\Delta\lambda$ and Δn_{eff} are the resonance wavelength change and the effective RI change, respectively. Since Δn_{eff} and n_{eff} are nearly the same for both OFRRs the common mode in both OFRRs can be tuned synchronously to ensure the single mode lasing over a broad spectral range. Fig. 2.9(a) shows such wavelength tuning by dissolving 2 mM R6G into the mixture of TEG and methanol (RI=1.36) whose RI can be varied by the proportion of methanol and TEG. As depicted in the inset of Fig. 2.9(a), the lasing wavelength clearly shows a linear relationship with the RI. To tune the lasing wavelength over an even large spectral range, a different dye solution can be injected to the same coupled OFRR structure. Fig. 2.9(b) shows the single mode lasing at 741.6 nm from the coupled OFRR using 2 mM LDS 722 in TEG.

2.4 Conclusion

In summary, we have experimentally demonstrated the single mode lasing from the coupled OFRR via the Vernier effect. The single mode operation is stable even under high pump energy density. It is not affected by the size of the laser cavity or the gain medium used, thus allowing us to use different sizes of the OFRRs for optimal lasing performance and to tune the lasing wavelength over various spectral ranges. Our study further shows that coupling between the OFRRs plays an important role in achieving the single mode lasing. Excessive coupling may spoil the Q-factor and result in incomplete side mode suppression. The tunable single mode lasing, low lasing threshold, cost-effective mass production, and the capability of coupling the lasing emission into a liquid channel make the PDMS based OFRR system a highly competitive technology in the development of optofluidic lasers and lab-on-a-chip devices.

Chapter III

A Quasi-droplet Optofluidic Ring Resonator Laser Utilizing a Micro-bubble

Optofluidic ring resonator lasers based on micro-bubbles filled with liquid gain medium are demonstrated. Due to the sub-micron wall thickness of the micro-bubble, significant amount of the electric field resides inside the liquid. Consequently, micro-bubbles mimic the droplets in air that have 3-dimensional optical confinement, extremely high Q-factors, and versatility in handling liquids of different refractive index. Furthermore, they enable repetitive interrogation and easy directional laser emission out-coupling without evaporation or size/shape variations. The laser using Rhodamine 6G in methanol is achieved with a threshold of 300 nJ/mm^2 and 5.3 μJ/mm^2 for 1 mM and 10 μM in concentration, respectively.

3.1 Introduction

Micro-droplets naturally integrate liquid and optical ring resonator, and thus are of great interest in the development of optofluidic devices, particularly, optofluidic lasers.(6, 20, 23) The micro-droplet supports the whispering gallery modes (WGMs), which circulate along the droplet surface and provide optical feedback for the gain medium dissolved in the droplet to lase.(20, 80, 81) Micro-droplet lasers have been

studied in 1980's and 1990's using free-falling or levitated droplets.(20, 82, 83) and recently using those formed on an ultra-hydrophobic surface.(65, 84, 85) They exhibit low lasing thresholds due to their extremely high Q-factors resulting from the smooth liquid-air interface and 3-dimensional light confinement, and are versatile in handling different liquids, in particular, water-based ones. However, those droplet lasers suffer from rapid liquid evaporation, lack of good control of size and shape, low efficiency of out-coupling into a waveguiding components (such as waveguide and optical fiber), and bulky droplet generators. These issues significantly hinder the development of the droplet lasers into a practically useful device.

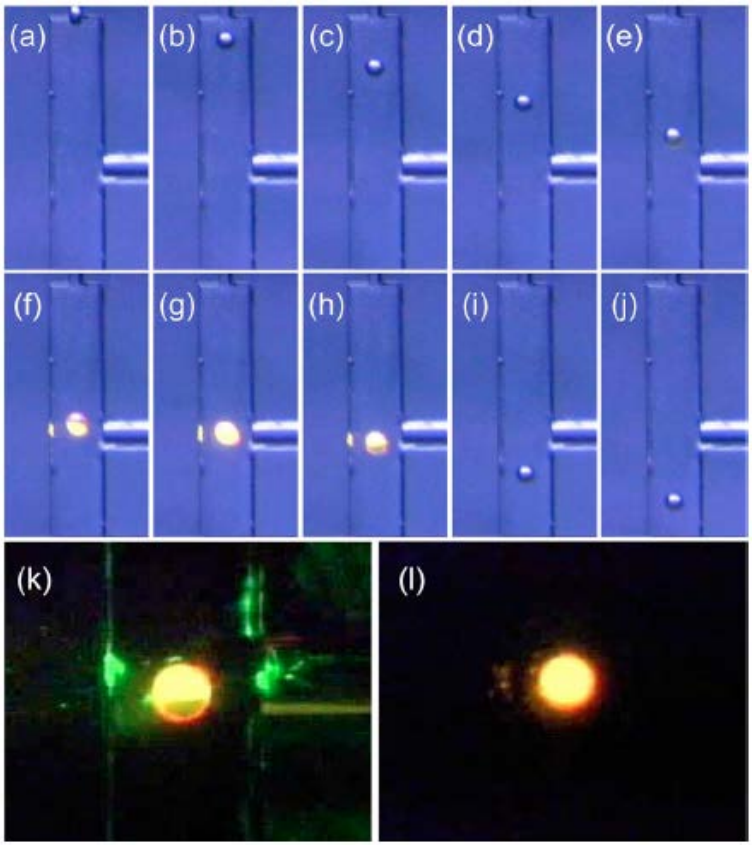

Figure 3.1 Free-falling microdroplet laser. Reprinted with permission from Ref. (86).

More recently, rapid generation of a large number of micro-droplets and subsequent demonstration of the corresponding droplet lasers have been achieved using microfluidics (such as T-junctions) with two immiscible liquids.(86-88) While those designs partially solve the aforementioned problems by miniaturizing the device and preventing evaporation of the liquid, new concerns emerge. Since droplets are surrounded by the carrier liquid, the refractive index (RI) of the droplet should be larger than that of the carrier fluid, which imposes considerable limitations in liquid selection.(86-90) In addition, the low RI contrast between the droplet and the carrier liquid significantly deteriorates the Q-factor.(86) In particular, for water based droplets (RI ~ 1.33), which are important for chemically and biologically related applications,(91-94) the RI contrast is too low that no laser emission is observed.(86) In addition, droplet size variation and shape deformation due to the perturbations during the droplet generation, and composition change due to the gradual mixing with the carrier liquid make the lasing characteristics less consistent.(88) Finally, the laser emission collection remains inefficient and inconvenient, as only the free-space coupling mechanism can be used.

In this chapter, we fabricate, characterize, and demonstrate a quasi-droplet optofluidic ring resonator (OFRR) laser based on a fused silica micro-bubble with an extremely thin wall. The bubble is formed by pressurizing a glass capillary under CO_2 irradiation.(95, 96) The wall thickness as thin as 560 nm is achieved. Consequently, when the bubble is filled with liquid, significant amount of the electric field of the WGM resides inside the liquid, thus making the composite micro-bubble and liquid system a quasi-droplet. The quasi-droplet laser has a number of advantages, as compared to the droplet laser discussed previously. (1) It mimics the droplet in air that provides excellent

Q-factors and 3-dimensional light confinement; (2) It is as versatile as the droplet in air and is capable of handling liquid of any RI; (3) It enables repetitive interrogation without any problems in evaporation, size variation, or shape deformation; (4) Its laser emission can be easily out-coupled through a waveguide or tapered optical fiber in contact with the bubble.

3.2 Fabrication

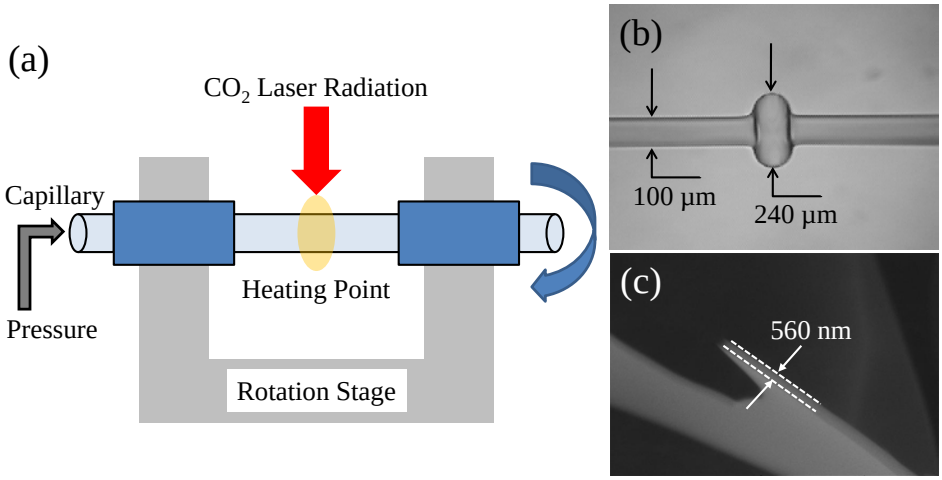

Figure 3.2 (a) Illustration of the setup for the micro-bubble fabrication. (b) Microscopic image of the micro-bubble made on the pre-etched capillary. The diameters of the micro-bubble and the capillary are 240 μm and 100 μm, respectively. (c) SEM image of the broken micro-bubble for measuring wall thickness. The thickness of the micro-bubble wall near the equator is 560 nm.

The fabrication processes of the micro-bubble are adapted from our previous work.(95, 96) First, we pre-etch a fused silica capillary, which has the outer diameter of 100 μm after conventional drawing,(7, 29) to obtain optimal wall thickness for the micro-bubble fabrication. After 5% aqueous hydrofluoric acid is flowed through the capillary for 2 hours, the wall thickness of the capillary is approximately 4.8 μm. We then connect the pre-etched capillary to the rotation stage with epoxy, and the capillary is pressurized and rotated under CO_2 laser radiation, as illustrated in Fig. 3.2(a). The CO_2 laser is tightly focused into a spot of a few hundred micrometers in diameter, and a portion of the capillary heated by the laser is blown up to form the micro-bubble. Fig. 3.2(b) shows the microscopic image of the micro-bubble with an outer diameter of 240 μm. In order to characterize the wall thickness, we break the micro-bubble and exam it under a scanning electron microscope (SEM). As shown in Fig. 3.2(c), the micro-bubble has a wall as thin

as 560 nm at its thinnest part (near the bubble equator). After the micro-bubble is formed on the capillary, fluidic channels are built at the both ends of capillary, enabling liquid flow through the capillary and micro-bubble as well. Note that using the similar blowing technology, the dead-ended micro-bubble has also been demonstrated very recently.(97) However, the flow-through structure reported here makes liquid delivery and replacement much easier, and is highly compatible with upstream and downstream micro-fluidics.

3.3 Theoretical study

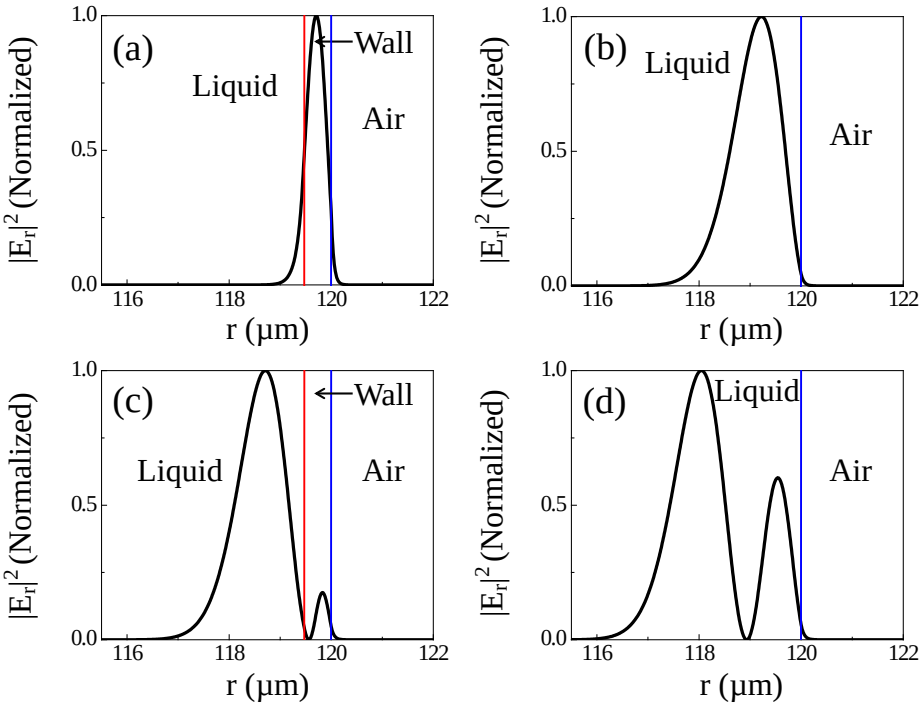

Figure 3.3 Calculated electric field distribution of the 1st (a, b) and 2nd (c, d) TM WGM in the radial direction in the micro-bubble (a, c) and the droplet (b, d). The radii of the micro-bubble and the droplet are both 120 μm, and the wall thickness of the micro-bubble is 560 nm, as illustrated by solid lines, respectively. Wavelength near 590 nm is used in the calculation and the micro-bubble is assumed to be a perfect hollow sphere filled with low index liquid (RI = 1.33). The electric field is normalized to the corresponding intensity peak.

The fraction of energy residing inside the low-index liquid core surrounded by the glass WGM resonator increases as the wall thickness decreases.(24) Since the liquid gain medium of our quasi-droplet laser is inside the fused silica micro-bubble, the wall should be thin enough to push the electric field into the liquid core in order to provide sufficient optical feedback for lasing. Fig. 3.3 plots the calculated electric field radial distribution of the transverse magnetic (TM) WGM of a micro-bubble filled with low index liquid (RI =

1.33) and the corresponding liquid droplet of the same size, respectively. Although for the 1st order mode, only 9.6% of the WGM resides inside the liquid core in contrast to over 99% of energy confined in the droplet, the fractional energy inside the liquid becomes nearly the same for the 2nd (and higher) order mode (96% vs. 99%), suggesting that the micro-bubble is virtually a droplet for those modes.

The Q-factor of a perfectly shaped micro-bubble resonator filled with the liquid is limited mainly by the absorption of the liquid, since the fused silica absorption loss is nearly negligible. It can be estimated using a relation $Q = 2\pi n/\eta\alpha\lambda$, where n, λ, α, and η are the effective refractive index, wavelength, attenuation coefficient of the liquid and the fraction of energy residing inside the liquid core, respectively. For methanol (the solvent used in our current quasi-droplet laser) and water, α is 5.9×10^{-4} cm^{-1} and 0.0035 cm^{-1} at 532 nm wavelength, respectively.(98) With η = 0.96, a Q-factor of our laser cavity of approximately 10^8 is achievable. Note that while experimentally such a high Q-factor can be characterized more accurately with cavity ring-down spectroscopy in the time domain,(99) our previous studies in the spectral domain on the micro-bubble resonator fabricated using the same method showed that a Q-factor exceeding 10^6 can be obtained, limited only by resolution of the spectrometer.(95, 96)

3.4 Experiments and results

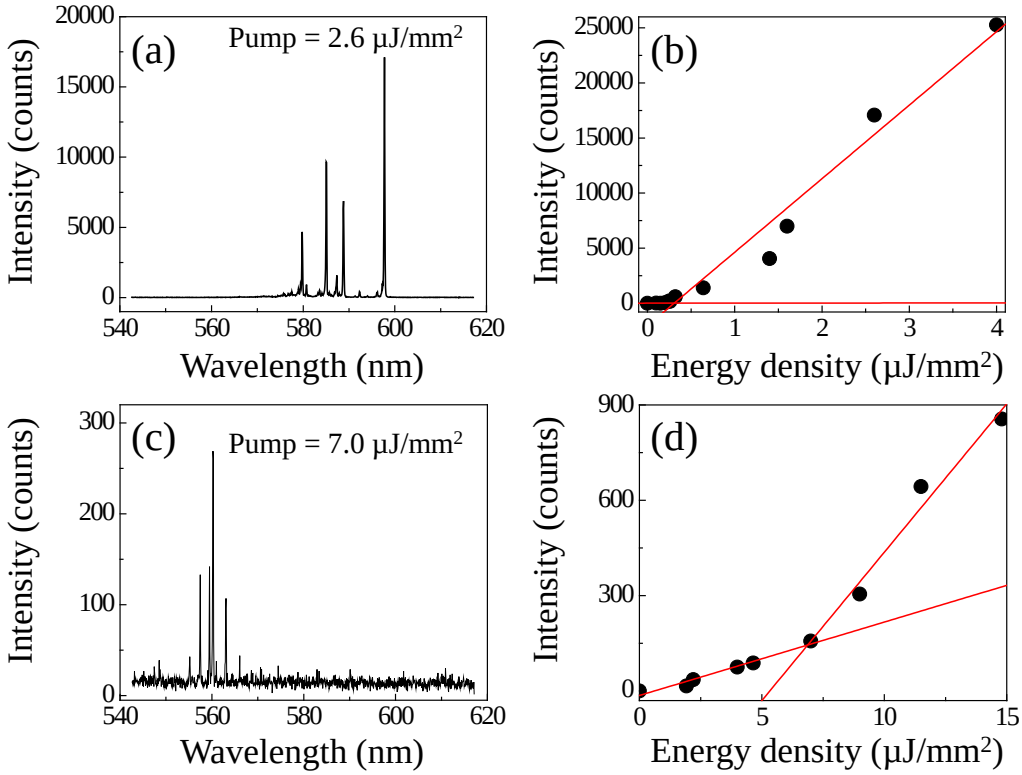

Figure 3.4 (a) Lasing spectrum of the quasi-droplet OFRR laser when 1 mM R6G dye dissolved in methanol is used as a liquid gain medium. (b) Corresponding intensity of the lasing emission as a function of the pump energy density. The threshold is approximately 300 nJ/mm^2. (c) Lasing spectrum of the same when the concentration of the R6G solution is reduced to 10 μM. (d) Lasing threshold curve corresponds to (c). The threshold is 5.3 μJ/mm^2. Solid lines in (b) and (d) are the linear fit for the dye emission below and above the lasing threshold.

To investigate lasing characteristics of our laser, we use Rhodamine 6G (R6G) dissolved in methanol, which has a RI (= 1.33) similar to that of water, as liquid gain medium. Utilizing the fluidic channel connected to the capillary, we flow the R6G solution through the micro-bubble with a flow-rate of 0.1 μL/min. The micro-bubble is optically pumped by a 5 ns pulsed optical parametric oscillator (OPO) at 532 nm with a frequency of 20 Hz. The lasing emission from the micro-bubble is then evanescently

coupled out via a tapered optical fiber in contact with the micro-bubble, and sent to a spectrometer (Horiba iHR550, resolution of 0.06 nm).

Fig. 3.4(a) shows the lasing spectrum of the quasi-droplet laser using 1 mM R6G solution, when the pump energy density is 2.6 μJ/mm^2. In contrast, the previous work shows no laser observed for such low RI droplets generated by microfluidics using two immiscible liquids due to very low RI contrast.(86) The laser emission ranges from 580 to 600 nm, similar to what is observed in droplet lasers.(64) The peak intensity of the laser as a function of the pump energy density is plotted in Fig. 3.4(b). The curve shows that the lasing threshold is approximately 300 nJ/mm^2, one order of magnitude lower than other optofluidic lasers (usually, a few μJ/mm^2), indicative of a high Q-factor of our quasi-droplet and strong light-gain medium interaction. Note that, due to the 3-dimensional light confinement, the number of the lasing peaks from the quasi-droplet OFRR laser is lower than that from a conventional micro-capillary based OFRR laser. These laser peaks emerge nearly simultaneously, as they have very similar lasing thresholds, as discussed previously.(68, 100) When the concentration of R6G solution is reduced to 10 μM, we obtain the lasing spectrum as depicted in Fig. 3.3(c), under the pump energy density of 7.0 μJ/mm^2. Note that the lasing wavelength blue-shifts due to the decrease in dye absorption.(68, 100) The corresponding lasing threshold curve is shown in Fig. 3.4(d) and shows that the threshold is increased to 5.3 μJ/mm^2, as expected.(68, 100)

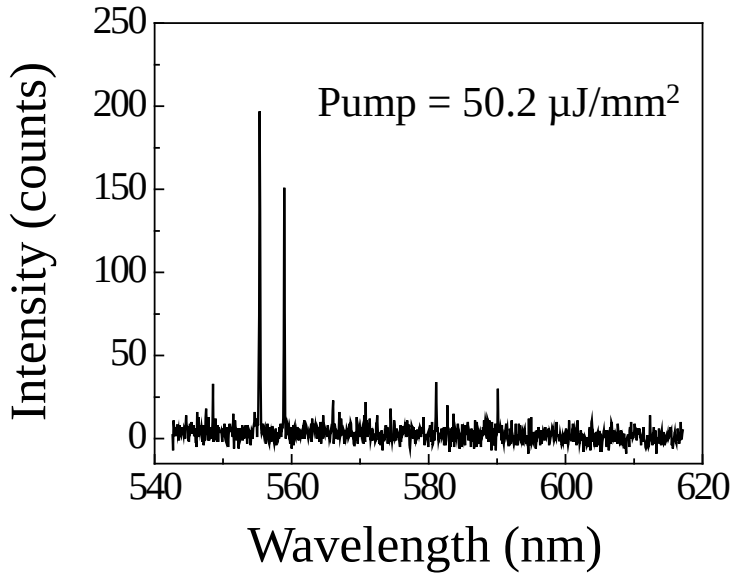

Figure 3.5 Lasing spectrum of the quasi-droplet OFRR laser with 1 μM R6G solution.

As low concentrations of dye solution are particularly important for bio/chemical sensing and biomedical applications of the OFRR lasers, we further decrease the R6G concentration. Fig. 3.5 shows that the laser emission can still be achieved even with 1 μM R6G solution. The corresponding lasing threshold is estimated to be approximately 20 $\mu J/mm^2$.

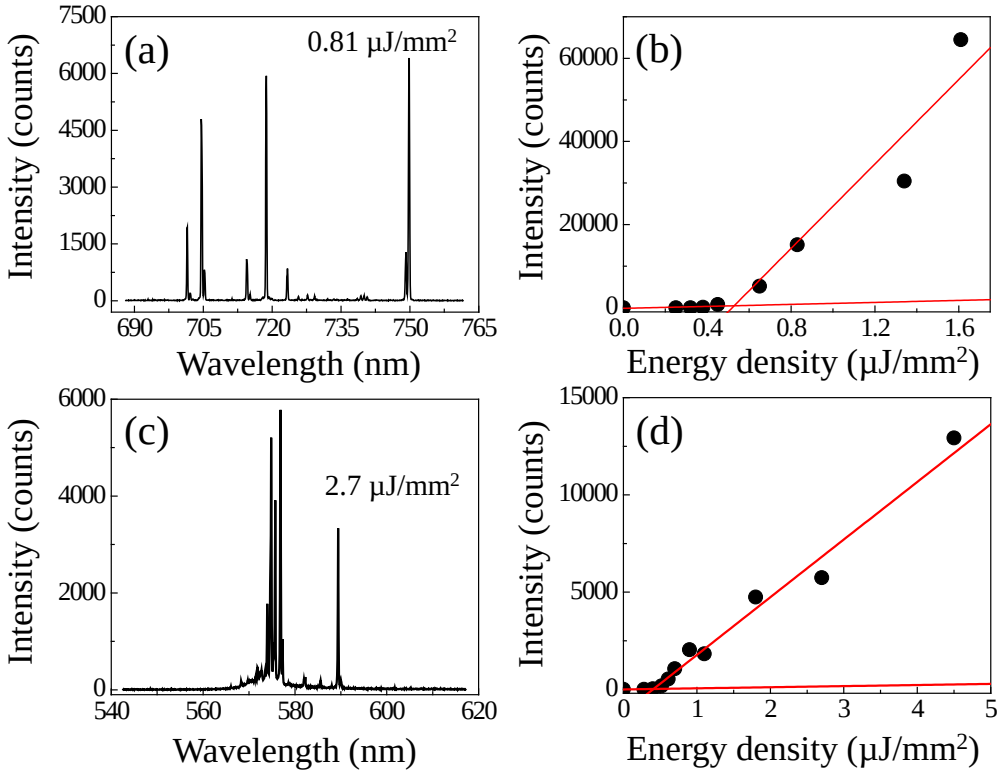

Figure 3.6 (a) Lasing spectrum of the quasi-droplet OFRR laser when 1 mM LDS722 dye dissolved in methanol is flowed through the micro-bubble. The pump energy density is 0.81 μJ/mm^2. (b) Corresponding threshold curve. The threshold is 0.52 μJ/mm^2. (c) Lasing spectrum of the same when 1 mM R6G dye dissolved in quinoline is flowed through the micro-bubble. The pump energy density is 2.7 μJ/mm^2. (d) Corresponding threshold curve. The threshold is approximately 400 nJ/mm^2. Solid lines in (b) and (d) are the linear fit for the dye emission below and above the lasing threshold.

Since our quasi-droplet laser has an advantage in liquid delivery, the dye solution filling out the micro-bubble can be easily replaced, which enables tuning of the lasing wavelength. As we switch the dye from R6G to LDS722, we are able to obtain the lasing emission using the same external pump source (532 nm). The corresponding lasing wavelength ranges from 700 to 750 nm, 150 nm longer than the R6G laser, as indicated in Fig. 3.6(a). The lasing threshold curve of 1 mM LDS722 laser is shown in Fig. 3.6(b), and the threshold of 0.52 μJ/mm^2 is obtained.

Moreover, the quasi-droplet laser mimics the droplet in the air, thus it can handle the liquid gain medium of any RI, as expected previously. Fig. 3.6(c) presents the lasing spectrum of the quasi-droplet laser when quinoline (RI ~ 1.626, larger than the RI of the wall) is used as a solvent to dissolve 1 mM R6G. The corresponding threshold is approximately 400 nJ/mm^2. Both the spectrum and the threshold are similar to those of the methanol laser with the same dye concentration [see Fig. 3.4(a) and (b)], suggesting that the fraction of the WGM interacting with the gain medium is similar, despite large RI difference between quinolone and methanol.

3.5 Discussion

In conclusion, we have demonstrated a quasi-droplet OFRR laser utilizing a fused silica micro-bubble fabricated on the capillary by CO_2 laser heating and blowing. The laser shows a very low lasing threshold due to a high Q-factor and strong light-matter interaction of the micro-bubble. Lasing is also achieved for a dye concentration as low as 1 μM. The lasing wavelength can be easily tuned by replacing the dye solution flowing through the micro-bubble. Furthermore, our quasi-droplet laser can utilize a dye solution with any RI as liquid gain medium, thanks to an extremely thin wall thickness of the micro-bubble. Finally, the quasi-droplet laser can be directionally out-coupled into a waveguide or fiber and can be interrogated repetitively, thus overcoming the problems associated with the free-falling droplets or the droplets generated via immiscible solutions. We envision that the quasi-droplet laser presented in this Letter will lead to a highly versatile technology for micro-total analysis systems and optofluidic light sources.

Chapter IV

Versatile Optofluidic Ring Resonator Lasers based on Microdroplets

We develop a novel nL-sized microdroplet laser based on the capillary optofluidic ring resonator (OFRR). The microdroplet is generated in a microfluidic channel using two immiscible fluids and is subsequently delivered to the capillary OFRR downstream. Despite the presence of the high refractive index (RI) carrier fluid, the lasing emission can still be achieved for the droplet formed by low RI solution. The lasing threshold of 1.54 μJ/mm2 is achieved, >6 times lower than the state-of-the-art, thanks to the high Q-factor of the OFRR. Furthermore, the lasing emission can be conveniently coupled into an optical fiber. Finally, tuning of the lasing wavelength is achieved via highly efficient fluorescence resonance energy transfer processes by merging two different dye droplets in the microfluidic channel. Versatility combined with improved lasing characteristics makes our OFRR droplet laser an attractive platform for high performance optofluidic lasers and bio/chemical sensing with small sample volumes.

4.1 Introduction

Despite the nL-sized cavity volumes of optofluidic laser devices, the actual consumption of samples (such as gain media or biological/chemical analytes) is quite large, since a continuous flow of liquid is used. As a result, a large fraction of samples is

wasted and the full potential of the optofluidic laser is not realized. Particularly, in the case where samples are very expensive or extremely low in abundance (such as in biological applications), utility of optofluidic lasers may be significantly hindered by the high cost associated with the sample consumption.

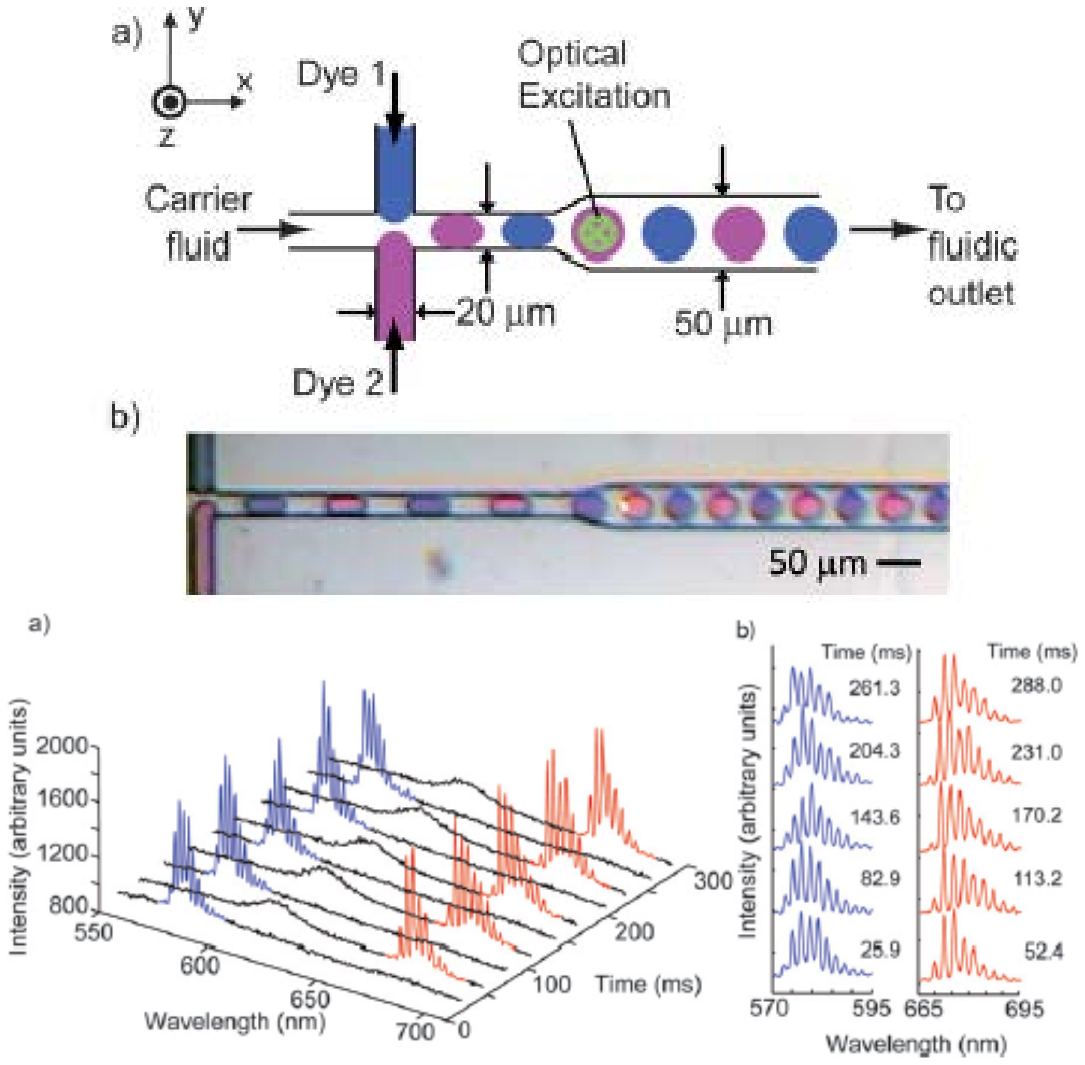

Figure 4.1 Microdroplet lasers inside a microfluidics channel. Reprinted with permission from Ref. (87).

Microdroplets have been investigated for years for biological/chemical sample delivery, analysis, and manipulation. (91, 92, 101) They naturally form liquid reaction

chambers of extremely low volumes (pL-nL). Moreover, using mature microfluidic technologies, microdroplets can be generated and stored in a large quantity, and can be manipulated (merged and split) individually on-demand. Introduction of microdroplets will render the optofluidic laser the highly desirable capabilities in sample delivery, manipulation, and controlled biological/chemical reaction.

Historically, the investigation of microdroplet lasers can be dated back in 1980's, when the free-falling or levitated droplets are used.(20) Recently, a few studies have been carried out on the microdroplet lasers inside a microfluidic channel using two immiscible liquids. For example, Tanyeri *et al.* obtained laser emission from a microdroplet of liquid dye surrounded by a low refractive index (RI) carrier fluid.(86) In this case, the droplet forms a ring resonator and supports the whispering gallery mode (WGM) that circulates along the droplet surface to provide the optical feedback. Similarly, through the T-junction microfluidics, rapid generation of the microdroplets and subsequent demonstration of laser emission are achieved, allowing for fast switching of the laser wavelength up to kilo-Hz (87). However, in the above designs, a few serious drawbacks still exist. First, the droplet is required to have a higher RI than the carrier fluid and no laser emission can be achieved for the droplet of lower RI (86, 87). Such requirement significantly limits the selection of the droplet liquid and the carrier fluid. In particular, for most biological applications, samples need to be the aqueous phase (RI = 1.33). Finding an immiscible carrier fluid with an RI sufficiently lower than that of water, would be very challenging. Second, the laser emission from those droplets can be collected only through scattering, thus greatly impairing the light detection efficiency. Third, the lasing spectrum may fluctuate due to the droplet size variations. Very recently,

laser emission from microdroplets in combination with an FP cavity is realized (19). This design employs the metal-coated facets of two optical fibers placed inside the microfluidic channel to form an FP cavity. It is capable of handling droplets of any RI and of coupling the droplet laser emission into the optical fiber with high efficiency. Consistent lasing spectrum can be obtained, as the cavity does not depend on the droplet size. However, due to the low Q-factor of the FP cavity, such a device usually has a high lasing threshold.

In this chapter, we investigate a novel nL-sized optofluidic laser scheme utilizing the capillary based OFRR that is connected to the upstream microdroplet generator (see Fig. 1). The OFRR consists of a thin-walled glass capillary. When the capillary is filled with solution, the circular cross section of the OFRR forms the ring resonator. The WGM circulates along the OFRR circumference and has the electric field present in both the liquid solution and the solid wall (102), thus providing the optical feedback for the gain medium flowing inside the capillary. The capillary based OFRR has a number of highly desirable features that overcome the aforementioned issues associated with other droplet lasers. First, it retains the advantage of the small sample volumes (~ nL) of the droplet. The OFRR cavity volume is on the order of only 1-10 nL. A single droplet can fill the entire cavity easily. Second, the lasing of the dye solution can be achieved regardless of the solution RI, even in the presence of the high RI carrier fluid (100, 102). Third, the lasing emission can be out-coupled efficiently into a waveguiding component (such as a waveguide or tapered optical fiber) in contact with the OFRR (71, 100, 102). Fourth, due to the high Q-factor of the OFRR (7, 93), a much lower lasing threshold can be obtained. Fifth, since the microdroplets utilize a solid-state OFRR cavity, it is free from the size

and shape variation, resulting in consistent lasing characteristics. Last, thanks to the nature of the capillary, the OFRR is highly compatible with the upstream and downstream microfluidics, thus providing convenient in-line sample analysis capability without interruption of the droplet flow. We first fabricate and characterize the droplet OFRR laser, and then show the lasing emission can be achieved with the low RI solution and with a lasing threshold >6 times lower than the state-of-the-art. Finally, we demonstrate the capability of the OFRR droplet laser in sample manipulation/analysis and in lasing wavelength tuning by merging two droplets containing respectively the donor and acceptor dyes.

4.2 Experiments

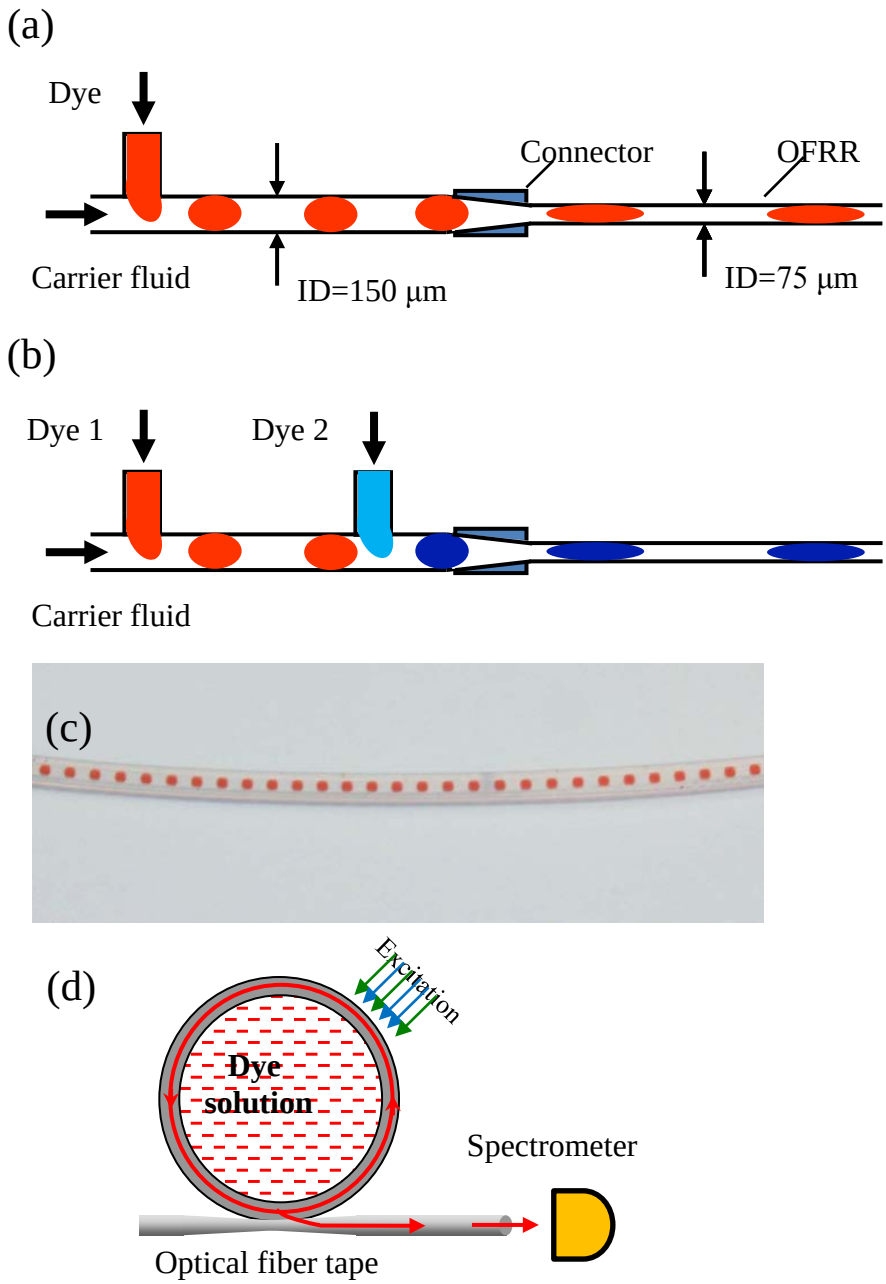

Figure 4.2 (a) Schematic of the droplet generating system consisting of a T-junction. The carrier fluid is silicone oil. The dye is dissolved methanol. The plastic tubing and the OFRR have an inner diameter (ID) of 150 µm and 75 µm, respectively. (b) Schematic of the droplet mixing system. (c) Picture of Rhodamine 6G droplet series generated inside a plastic tubing. (d) Cross-sectional view of the OFRR and the laser excitation and out-coupling.

The droplet generation system, schematically shown in Fig. 4.2(a), is adapted from the work by Trivedi *et al.* (101). It consists of plastic tubings (Upchurch, P1476, inner diameter (ID) = 150 μm) and a T-junction (Upchurch, P-890). The hydrophilic phase consists of Rhodamine 6G (R6G) (Exciton Inc.) dissolved in methanol (RI = 1.33). The hydrophobic carrier fluid is silicone oil (Dow Corning 200 Fluid, RI = 1.53) with viscosity of 10 centistokes. The methanol phase and the carrier fluid are injected by the syringe pumps (KD Scientific) at a respective flow rate of Q_d = 3 μL/min, and Q_o = 10 μL/min. When continuous liquid flows meet at the T-junction, a series of methanol droplets separated by immiscible silicone oil form at a rate of 0.4 Hz. Each droplet is approximately 125 nL in volume and fills the entire cross section of the tubing. Fig. 4.2(b) illustrates the droplet generation and mixing system, which consists of a second T-junction downstream. R6G and LDS 722 (Exciton Inc.), both dissolved in methanol, are used as Dye 1 and Dye 2, respectively, with a flow rate of 3 μL/min for each. As both R6G and LDS 722 have the same solvent (methanol), they can easily mix together and form a larger droplet. Fig. 4.2(c) shows, as an example, the picture of a series of R6G droplets stored inside a plastic tubing.

We fabricate the capillary OFRR by the conventional drawing method (7, 29). A fused silica capillary with the original ID of 536 μm and the wall thickness of 40 μm is mechanically pulled under CO_2 laser irradiation. The resultant OFRR is approximately 3 cm long, 75 μm in ID, and about 7 μm in wall thickness. It can be connected easily to the outlet of the plastic tubing, as illustrated in Figs 4.2(a) and (b). Fig. 4.2(d) depicts the cross-sectional view of the OFRR. Inside the OFRR, the droplet becomes elongated (due to the small inner diameter in comparison with the plastic tubing) and fills the entire

cross-section of the OFRR. An optical parametric oscillator (Continuum, 532 nm, 5 ns pulse width, 20 Hz repetition rate) is focused on the side of the OFRR. An optical fiber taper is in contact with the OFRR and couple the laser emission efficiently into a spectrometer (Horiba iHR550, resolution of 0.06 nm) at the distal end.

4.3 Results and discussion

4.3.1 Comparison with conventional OFRR laser

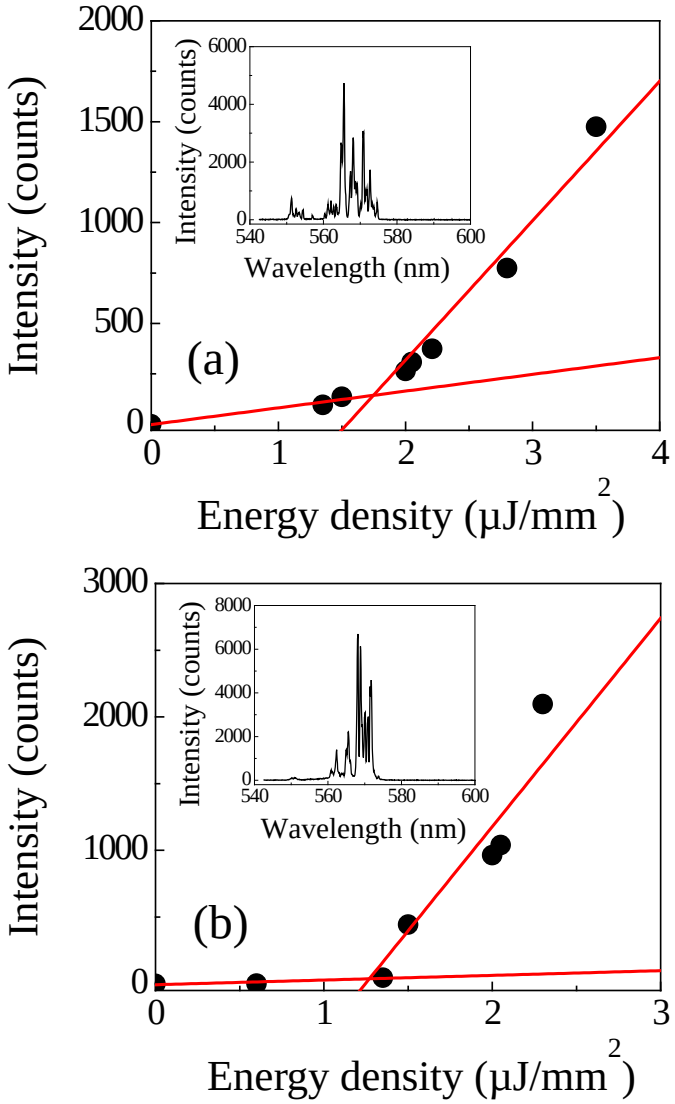

Figure 4.3 (a) Lasing intensity from the micro-droplet flowing through the OFRR as a function of pump energy density. 1mM Rhodamine 6G dye dissolved in methanol forms the droplet in the carrier fluid, and the micro-droplet gain medium is pumped by pulsed laser (532 nm, 20 Hz). The lasing threshold is approximately 1.54 μJ/mm2. Inset shows the lasing spectrum when the pump energy density is 6.5 μJ/mm2. (b) The lasing threshold curve of a conventional continuous flow OFRR laser with the same dye concentration. The threshold is 1.25 μJ/mm2, and the lasing signal at the pump energy density of 6.2 μJ/mm2 shows similar spectrum with (a), as illustrated in the inset.

Since the OFRR wall (fused silica) has a higher RI than the dye solution (methanol), the majority of the WGM resides inside the wall and only the evanescent field of the WGM interacts with the liquid gain medium. Thus, it is imperative that the high RI layer of the carrier fluid (silicon oil) sandwiched between the dye solution and the OFRR wall be sufficiently thin (less than several micrometers) so that the strong WGM-dye interaction can be sustained. Previous studies with the dye droplet surrounded by a thick layer of high RI oil show that no lasing emission can be achieved (86, 87). Since the OFRR inner surface is hydrophilic, we expect that, in the presence of methanol, hydrophobic oil should be expelled away from the OFRR inner surface. As a result, the dye solution should fill nearly the entire of the OFRR cross section (see Fig. 4.3(d)). To test this, we carry out two experiments. The first experiment is shown in Fig. 4.3(a). When the R6G/methanol droplet in the carrier fluid flows through the OFRR, under the external excitation the typical multi-mode laser emission ranging from 550 nm to 580 nm emerges, which can be out-coupled by a tapered optical fiber in contact with the OFRR (see the inset of Fig. 4.3(a)). The lasing threshold, based on the maximum intensity of the lasing signal as a function of the pump energy, is measured to be approximately 1.54 $\mu J/mm^2$. The results presented above show that using our OFRR system the droplet lasing can be achieved even in the presence of high RI oil and with a much lower lasing threshold (>6 times), which represent a significant advance over the droplet laser systems previously reported (19, 86, 87).

As a control experiment, R6G in methanol alone is flowed through the same OFRR continuously. The lasing characteristics of the conventional OFRR dye laser are presented in Fig. 2(b). It has a similar lasing threshold of 1.25 $\mu J/mm^2$, and shows nearly

the same lasing spectrum as in our OFRR droplet dye laser. Comparison between the results in Figs. 4.3(a) and (b) suggests that, while the exact thickness of the oil layer between the dye solution and the OFRR wall is unknown, it must be optically thin (less than one wavelength) and the existence of the oil layer (if any) does not alter noticeably the interaction between the WGM and the dye. Consequently, the OFRR droplet laser should be similar to the continuous flow OFRR laser and a number of advantageous characteristics of the OFRR, such as lasing emission with low RI solution, the high Q-factor ($>10^7$ (7, 93)), and the high out-coupling efficiency (>50% (71)), can be kept.

4.3.2 Time-discrete laser emission

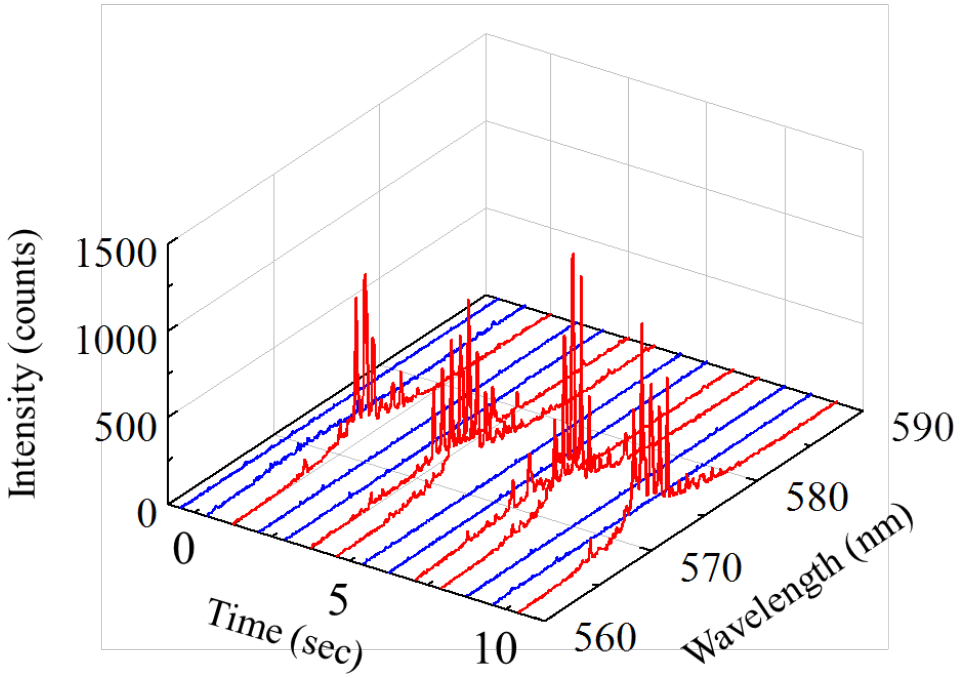

Figure 4.4 (a) Lasing spectra from the micro-droplet laser as a function of time. As the R6G/methanol droplet flows through the capillary OFRR with the gap formed with silicon oil, the laser shows pulsed lasing signal at the frequency of 0.4 Hz. Note that the signals from the carrier fluid gap between different droplets are zero.

As the pump laser is focused only on a small portion of the OFRR, the device should exhibit the lasing emission only when the droplet passes through the focusing point. Fig. 4.4 plots the lasing signal from the OFRR droplet laser as a function of time, when 1 mM R6G droplet and the carrier fluid are flowed through the OFRR. With the flow rate of 13 μL/min (Q_d = 3 μL/min, Q_o = 10 μL/min), the lasing signal at the frequency of 0.4 Hz is obtained. It is clearly seen that the lasing signal is observed only from the dye droplet and the signals from the carrier fluid gap between two adjacent

droplets are virtually zero. Therefore, it is possible to distinguish two different droplets by the carrier fluid gap in our system, which is essential for individually analyzing and manipulating the droplets. Note that although the tuning frequency reported here is much lower that previous studies (19, 87), when needed, it can be increased drastically by using different microfluidic channel geometries and flow rates.

4.3.3 FRET lasing

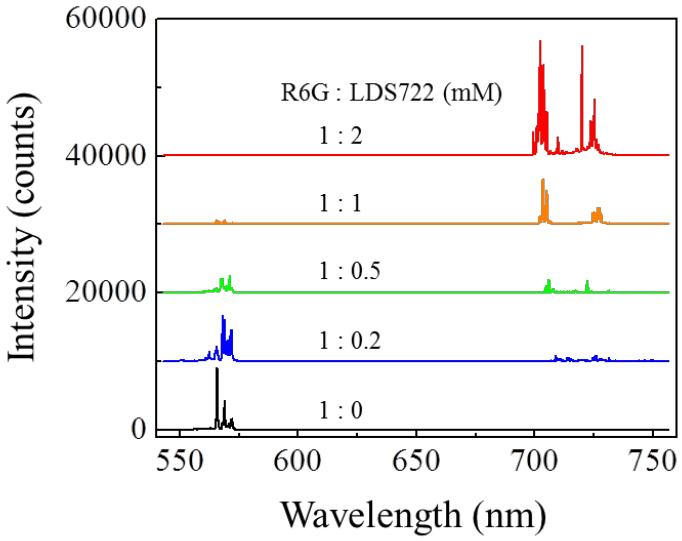

Figure 4.5 FRET lasing spectra from mixed droplets with various donor/acceptor concentrations. R6G and LDS722 are used as the donor and the acceptor, respectively. The concentration of the donor is fixed to 1 mM and the concentration of the acceptor varies from 0 to 2 mM as indicated. Curves are vertically shifted for clarity. The pump energy density is 14.6 μJ/mm^2 for all cases. As the concentration of the acceptor increases, the donor lasing signal around 570 nm wavelength diminishes, and the acceptor lasing signal ranges from 700 nm to 740 nm arises.

As discussed earlier, microdroplets serve as an excellent chemical and biological reaction chamber and can be manipulated conveniently. The droplet and the OFRR in combination will provide powerful capability in sample generation, delivery, processing, and in-line analysis. Here, we demonstrate the rapid sample mixing of donor dye (R6G) and acceptor dye (LDS722) in two droplets and subsequently achieve the tuning of the lasing wavelength through the fluorescence resonance energy transfer (FRET) between the donor and the acceptor.(103) The experimental setup is described in Fig. 4.3(b) where two different dyes are merged into a single microdroplet by two T-junctions. During the

experiment, the LDS722 concentration is varied whereas the R6G concentration remains at 1 mM. Since the Förster distance between R6G and LDS722 is about 6.2 nm (104), significant energy transfer is expected to occur when LDS722 concentration is above 1 mM. Fig. 4.5 shows the lasing spectra from merged droplets with various R6G/LDS722 ratios. In the absence of LDS722, the droplet OFRR laser shows a typical R6G lasing signal in the 550 to 580 nm range. With the increased LDS722 concentration, due to the FRET process, the lasing emission in the LDS722 range (710 – 740 nm) starts to emerge whereas the R6G lasing emission decreases. With 2 mM LDS722 concentration, the donor emission is completely suppressed and strong lasing emission from LDS722 is observed. While in the above experiment, only 150 nm wavelength tuning is demonstrated, larger wavelength tuning is certainly possible by implementing cascade energy transfer processes where three or more dyes can be mixed. Note that, due to the nature of the droplet, sample mixing is rapid, as evidenced by the decrease (or disappearance) of the donor lasing emission and the concomitant emergence of the acceptor lasing emission within a few seconds after mixing.

4.4 Conclusion

In summary, we demonstrate a novel microfluidic laser that combines microdroplets and the capillary based optofluidic ring resonator with a high Q-factor. This device has nL-sized sample and cavity volume and is versatile in handling solutions of various RIs. In particular, the lasing emission can be obtained even in the presence of high RI carrier fluid. A lasing threshold of 1.54 $\mu J/mm^2$ is achieved, much lower than the state-of-the-art. By mixing two droplets containing respectively the donor dye and acceptor dye, we not only demonstrate the OFRR droplet laser's capability in tuning or switching of the lasing wavelength, but also open the door to the potential biosensing applications of the OFRR droplet laser (93, 94).

Chapter V

Intracavity DNA Melting Analysis with Optofluidic Lasers

DNA melting analysis holds great promise for simple and fast DNA sequence discrimination. However, conventional fluorescence-based methods suffer from a small differential signal and demanding melting curve analysis, both of which make it diffcult to distinguish the target DNA from the mismatched one. Herein, we propose and demonstrate a highly specific intracavity DNA melting analysis scheme utilizing an optofluidic laser. The laser optically amplifies the small yet intrinsic thermal dynamic difference between the target and the single-base-mismatched DNA, resulting in a differential signal that is orders of magnitude greater than with fluorescence-based methods. In particular, the existence of a phase transition between the stimulated laser emission and fluorescence (i.e., spontaneous emission) enables accurate determination of the DNA transition temperature difference. Furthermore, the high differential signal in the intracavity detection allows for scanning of the laser excitation at a fixed temperature to distinguish two DNA sequences, which provides another means for rapid DNA analysis. In this paper, we first theoretically investigate DNA melting analysis using an optofluidic laser and then experimentally explore this scheme with a highquality optofluidic ring resonator. Distinction of two DNA sequences of up to 100 bases long is

demonstrated. The intracavity detection developed here will lead to novel optofluidic devices that enable rapid and simple analysis of DNAs with very long sequences.

5.1 Introduction

5.1.1 DNA sequence analysis

For a few decades, considerable efforts have been made to develop DNA analyzers, owing to the key role of DNA in the transfer of genetic information.(48, 49) A DNA sequence may have a single-base change resulting from biological processes such as single point mutation or cytosine methylation. Distinguishing the sequence difference at the level of single-base-mismatch in DNAs can provide valuable information for disease diagnosis, medicine development, and genomic research.(3, 44, 45, 47, 50, 105, 106) In particular, it is important to detect and monitor the polymorphism, which is caused by mutation, for medical and food diagnosis, environmental control, and homeland security. Many technological advances have been made to provide us with the tools to analyze single base-mismatch. Most of those technologies utilize fluorescence from the dye labeled on a DNA probe, which adds costs and detection processes.

5.1.2 Hybridization-based methods

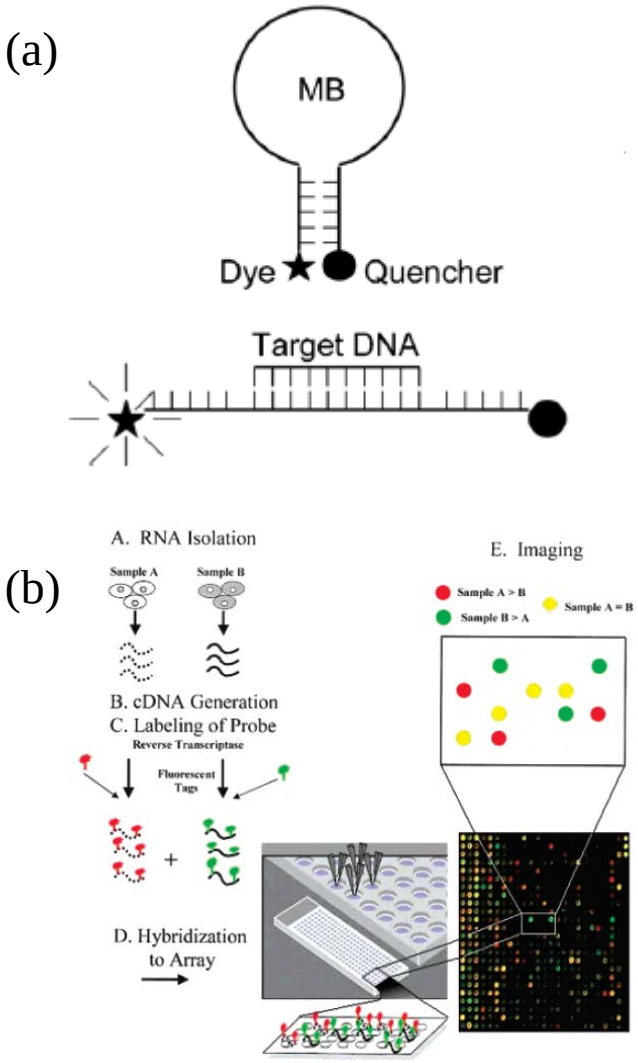

Figure 5.1 (a) Detection of target DNA using Molecular beacon. (b) DNA array on chip. Reprinted from Ref. (51, 62) with permission.

As DNA molecules consist of base pairs, DNA sequences can be detected utilizing the hybridization of the DNA strands. Fig. 5.1 shows widely used methods detecting DNA sequence in interest based on the hybridization.(51, 62) The methods usually rely on a fluorescence signal from dye-labeled DNA probes. The target DNA modifies distance between the dye and the quencher within the DNA probe with a form

of molecular beacon, resulting in changes in the fluorescence signal from the sample. When DNA probes are immobilized to the substrate in other hand, an optical signal from the DNA array chip can be used to monitor hybridization of DNA sequences. As compared to an enzyme-based DNA sequence analysis, the hybridization-based methods are simple and fast.

However, the hybridization-based methods include labeling to the DNA probes with fluorescent dye molecules, which add cost and complexity to the entire process. DNA molecular beacon can analyze sequences only with limited base pairs, since a long strand cannot form the molecular beacon. DNA arrays and other optical detection methods need immobilization of DNA probes into the substrate which also increase costs.

5.1.3 DNA melting analysis

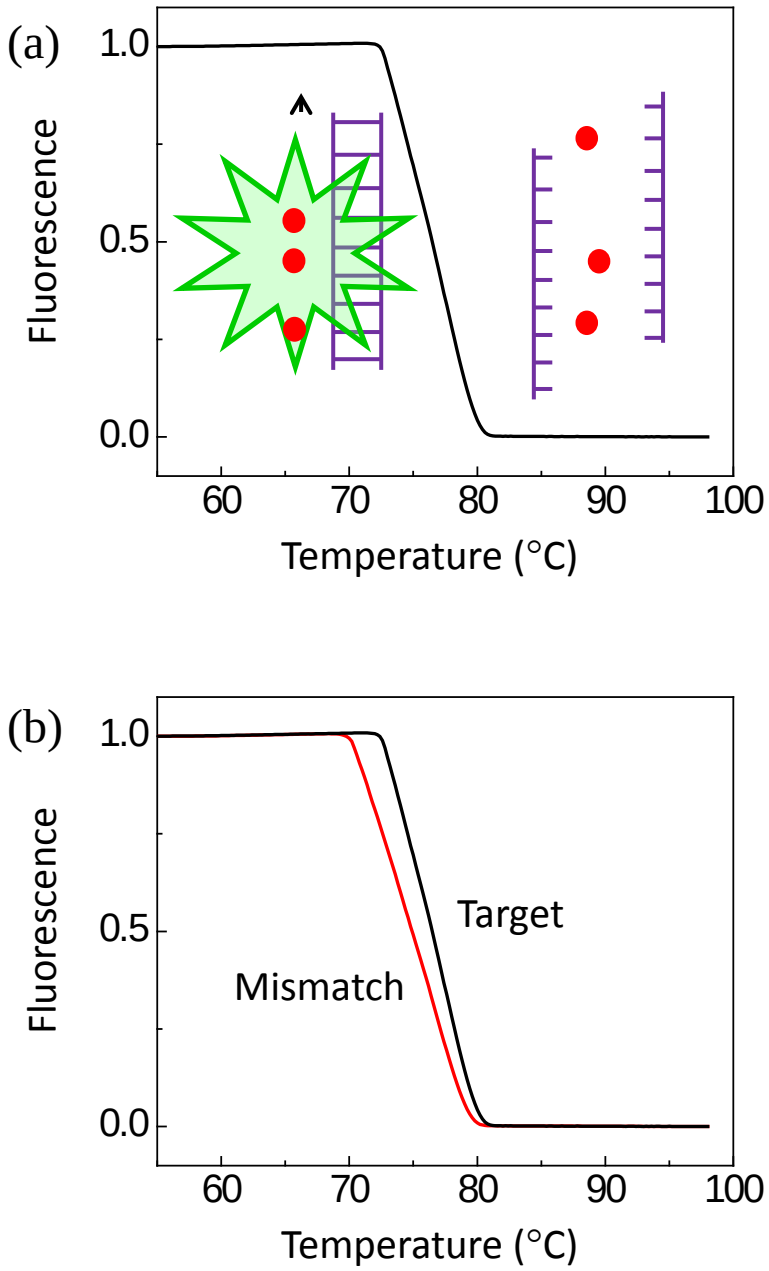

Figure 5.2 (a) Concept of HRM analysis. (b) Discrimination of target and base-mismatched DNA.

Nucleic acid thermodynamics studies an effect of temperature on the double-stranded DNA (dsDNA).(42, 43, 50) The dsDNA is bound by a bonding energy of base

pair, thus it can be melt down into single-stranded DNA (ssDNA) when thermal energy exceeds the bonding energy.

High resolution melting (HRM) analysis is a newly developed technology for analyzing DNA, in particular, after polymerase chain reaction (post-PCR) (107-111), in a contamination-free closed-tube manner.(44, 45, 47, 56-61, 112) It is a unique technology that relies on intercalating saturation dyes to monitor double-stranded DNA (dsDNA). Saturation dye has a very high fluorescence quantum yield in the presence of dsDNA, but its quantum yield diminishes when dsDNA becomes single-stranded DNA (ssDNA) at relatively high temperature. HRM uses the saturation dye directly and does not require any costly labeling processes. Therefore, it is a powerful method to discriminate base-mismatches. HRM relies on the thermal dynamic difference between the target and the single-base-mismatched DNA to distinguish them. As illustrated in Fig. 5.2, HRM employs fluorescence from intercalating saturation dyes as the sensing signal. The saturation dye, when bound to double-stranded DNA (dsDNA), has strong fluorescence. With increased temperature, dsDNA dissociates into a single-stranded DNA (ssDNA). As a result, the dye is released from the dsDNA strands and its fluorescence decreases. The DNA melting curve is acquired by monitoring the fluorescence as a function of temperature. The melting curve depends on the affinity between the two binding DNA strands, which is in turn determined by the length and the sequence of the DNA, as well as the number of base mismatches.

As compared to other DNA analysis methods, such as molecular beacons and DNA arrays (51, 54), HRM is simple, fast, cost-effective, and easy to use. It does not require complicated and costly fluorophore labeling and can be directly operated in free

solution without involving surface immobilization of DNA probes. Particularly, in contrast to the molecular beacons and DNA arrays that handle only short DNA sequences (~20-30 bases), HRM is capable of analyzing DNA sequences of hundreds of bases. To date, HRM has been employed in single nucleotide polymorphisms, mutation discovery, and viral/bacterial population diversity investigation.

However, due to the small thermal dynamic difference between the target and mismatched DNA, the difference in fluorescence signal is usually very small (a few percent) and diminishes with the increased sequence length. Finding an optimized method to resolve the small yet intrinsic thermal dynamic difference is crucial in expanding the HRM capability for DNA analysis. HRM has to scan the temperature to differentiate the base-mismatch from the target, which makes the overall detection slow. In addition, the fluorescence difference between the target DNA and the single-base mismatched DNA is small, which affects the HRM's capability in differentiating mismatch.

In this chapter, we demonstrate a lasing from the saturation dye in the presence of dsDNA, and propose a novel technique for rapid and direct detection of the target DNA and the base-mismatched DNA. Sample solution containing the saturation dye and the probe ssDNA is mixed with different DNA sequences, and is analyzed with a downstream optofluidic laser. Clear difference in lasing characteristics from the target and the single base mismatched DNA is observed.

5.2 Our approach

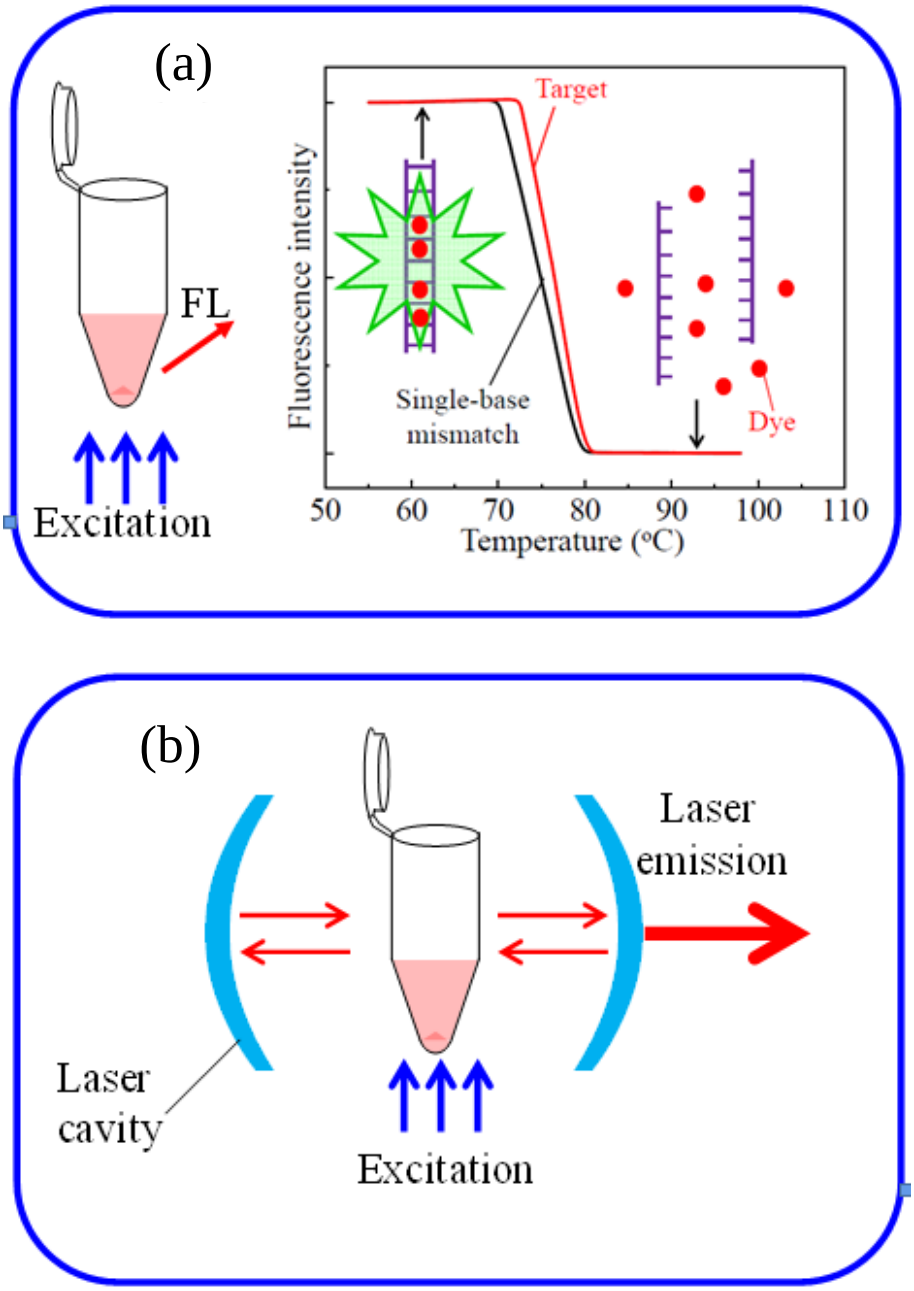

Figure 5.3 (a) Conventional HRM analysis. (b) Idea of DNA melting analysis based on laser.

We attempt to amplify the thermodynamic difference using an optical feedback provided by a laser cavity as shown in Fig. 5.3. Our scheme involves placing DNA

samples and saturation dyes inside an optofluidic laser cavity for intra-cavity detection. Instead of fluorescence, stimulated emission from a laser is used as the sensing signal. When temperature varies the laser gain and hence the laser output, which is determined by the DNA hybridization state, is modulated significantly. Our scheme offers a number of unique advantages: (1) Through an intra-cavity detection, the small yet intrinsic thermal dynamic difference between the target and the single-base mismatched DNA can be optically amplified, resulting in orders of magnitude improvement in differential signal (the ratio between the fluorescence from the target and mismatched DNA); (2) When temperature varies, the laser undergoes a sharp phase transition from stimulated laser emission to regular fluorescence (i.e., spontaneous emission), which allows us to accurately define and precisely determine the DNA transition temperature; (3) In addition to temperature ramping as in the conventional melting analysis, the high differential signal allows to scan the laser excitation at a fixed temperature to distinguish two DNA sequences, which provides another means for rapid DNA analysis. In this paper, we first theoretically investigate DNA melting analysis using an optofluidic laser and then experimentally demonstrate this scheme with an optofluidic ring resonator (OFRR).

5.3 Theoretical study

5.3.1 Calculation of dsDNA fraction

Γ is the fraction of the saturation dye molecules that contribute to lasing as well as fluorescence, and can be presented by:

$$\Gamma = \frac{n_{dsDNA}}{n_T} \tag{5.1}$$

where n_T is the total concentration of the dye and n_{dsDNA} is the concentration of the dye that binds to dsDNA, which is proportional to the dsDNA concentration. To determine the concentration of the dsDNA formed from ssDNAs, the hybridization reaction is first expressed by:

$$[ssDNA1] + [ssDNA2] \leftrightarrow [dsDNA], \tag{5.2}$$

while the equilibrium constant K_d for this reaction can be obtained by:

$$K_d = \frac{[dsDNA]}{[ssDNA1][ssDNA2]}. \tag{5.3}$$

According to thermodynamics,(42, 43) the relation between the binding energy (change in Gibbs free energy), ΔG, and K_d is

$$\Delta G = -RT \ln K_d \tag{5.4}$$

where R is the ideal gas constant and T is temperature.

Assuming that there is same number of the ssDNA1 and the ssDNA2;

$$[ssDNA1] = [ssDNA2], \tag{5.5}$$

and the total number of ssDNA copies remains same through the reaction (as same as our experimental conditions);

$$[dsDNA] = 1-[ssDNA1] = 1-[ssDNA2], \tag{5.6}$$

Γ can be obtained by combining (5.1), (5.3) and (5.4):

$$\Gamma = 1 - \left(\frac{e^{\frac{\Delta G}{RT}}}{2} \left(-1 + \sqrt{1 + 4e^{-\frac{\Delta G}{RT}}} \right) \right). \quad (5.7)$$

On the other hand, ΔG can be calculated by nearest neighbor method.(113) ΔG is given by:

$$\Delta G^0(\text{total}) = \Delta H^0_{\text{total}} - T\Delta S^0_{\text{total}}, \quad (5.8)$$

where enthalpic, ΔH, and entropic, ΔS, parameters can be determined for the ten possible base pair patterns given in Table 5.2.(113) As the DNA sequences of our 21, 40 and 100 bases-long DNAs are given in Table 5.1, ΔG can be calculated and plugged into Eq. 5.7 to calculate Γ as a function of temperature. Γ obtained here can be directly used in our calculations for the laser thresholds, outputs and fluorescence signals.

Table 5.1 DNA sequences used in the calculations/experiments

Length of DNAs	Sample Description	Sequence (Red character denotes intentional base mismatch.)
21 bases	Target	5'-ACA ACA AAG AAC ATA CAT AGG-3'
		5'-CCT ATG TAT GTT CTT TGT TGT-3'
	Mismatch	5'-ACA ACA AAG AAC ATA CAT AGG-3'
		5'-CCT ATG TAT ATT CTT TGT TGT-3'
40 bases	Target	5'-ACA ACA AAG AAC AAA TAT ACA TAT ATG ATA TAA CAA CAA A-3'
		5'-TTT GTT GTT ATA TCA TAT ATG TAT ATT TGT TCT TTG TTG T-3'
	Mismatch	5'-ACA ACA AAG AAC AAA TAT ACA TAT ATG ATA TAA CAA CAA A-3'
		5'-TTT GTT GTT ATA TCA TAT ATA TAT ATT TGT TCT TTG TTG T-3'
100 bases	Target	5'-AAA AAC AAA AAA CAA AAA AAA CAA AAA AAA AAC AAA AAA AAA AAA AAA ACA AAA AAA AAA AAC AAA AAA CAA AAA CAA AAA AAA AAA CAA AAA CAA AAA A-3'
		5'-TTT TTT GTT TTT GTT TTT TTT TTT GTT TTT GTT TTT TGT TTT TTT TTT TTG TTT TTT TTT TTT TTT TGT TTT TTT TTT GTT TTT TTT GTT TTT TGT TTT T-3'
	Mismatch	5'-AAA AAC AAA AAA CAA AAA AAA CAA AAA AAA AAC AAA AAA AAA AAA AAA ACA AAA AAA AAA AAC AAA AAA CAA AAA CAA AAA AAA AAA CAA AAA CAA AAA A-3'
		5'-TTT TTT GTT TTT GTT TTT TTT TTT GTT TTT GTT TTT TGT TTT TTT TTT TTA TTT TTT TTT TTT TTT TGT TTT TTT TTT GTT TTT TTT GTT TTT TGT TTT T-3'

Table 5.2 Nearest-neighbor parameters for base pair patterns

Nearest-neighbor sequence (5'-3'/3'-5')	$\Delta H°$ (kJ/mol)	$\Delta S°$ (J/(mol·K))
AA/TT	-33.1	-92.9
AT/TA	-30.1	-85.4
TA/AT	-30.1	-89.1
CA/GT	-35.6	-95.0
GT/CA	-35.1	-93.7
CT/GA	-32.6	-87.9
GA/CT	-34.3	-92.9
CG/GC	-44.4	-113.8
GC/CG	-41.0	-102.1
GG/CC	-33.5	-83.3
Terminal A-T base pair	9.6	17.2
Terminal G-C base pair	0.4	-11.7

5.3.2 Laser threshold and output

According to the laser theory (114), the lasing threshold, I_{th}, is determined by:

$$I_{th} = \frac{\gamma}{\Gamma - \gamma}, \tag{5.9}$$

where g is the required fraction of the dye molecules in the excited state at the onset of lasing, which is determined by the properties of the dye (such as dye absorption/emission cross section and total concentration) and the laser cavity (such as Q-factor).(6, 62, 68, 100) Γ is the fraction of the dye molecules that contribute to the lasing, i.e.:

$$\Gamma = \frac{n_{dsDNA}}{n_T}, \tag{5.10}$$

where n_T is the total concentration of the dye. n_{dsDNA} is the concentration of the dye that binds to the dsDNA and should be proportional to the dsDNA concentration, [dsDNA], which is in turn given by:

$$[dsDNA] \overset{K_d}{\Leftrightarrow} [ssDNA], \tag{5.11}$$

where K_d is the temperature dependent dissociation constant and can be calculated using the standard method based on nearest-neighbor thermal dynamics for any given DNA sequence and temperature. Detailed calculation of Γ is described in the previous chapter. For the laser output intensity, it is linearly proportional to the external pump energy level, I_{pump}, above the lasing threshold, i.e.:

$$I_{output} \propto (\frac{I_{pump}}{I_{th}} - 1) = I_{pump} \times (\frac{\Gamma}{\gamma} - 1) - 1. \tag{5.12}$$

Through Eq. (5.9)-(5.12), we can gain insight into how the optofluidic laser can be controlled by DNA thermodynamics. Note that Γ also reflects the fluorescence intensity from the dye in the conventional DNA melting analysis, i.e.,

$$I_{output} \propto \Gamma. \tag{5.13}$$

Eqs. (5.12) and (5.13) allow us to compare the melting curves obtained with the intra-cavity detection and the conventional fluorescence method, respectively.

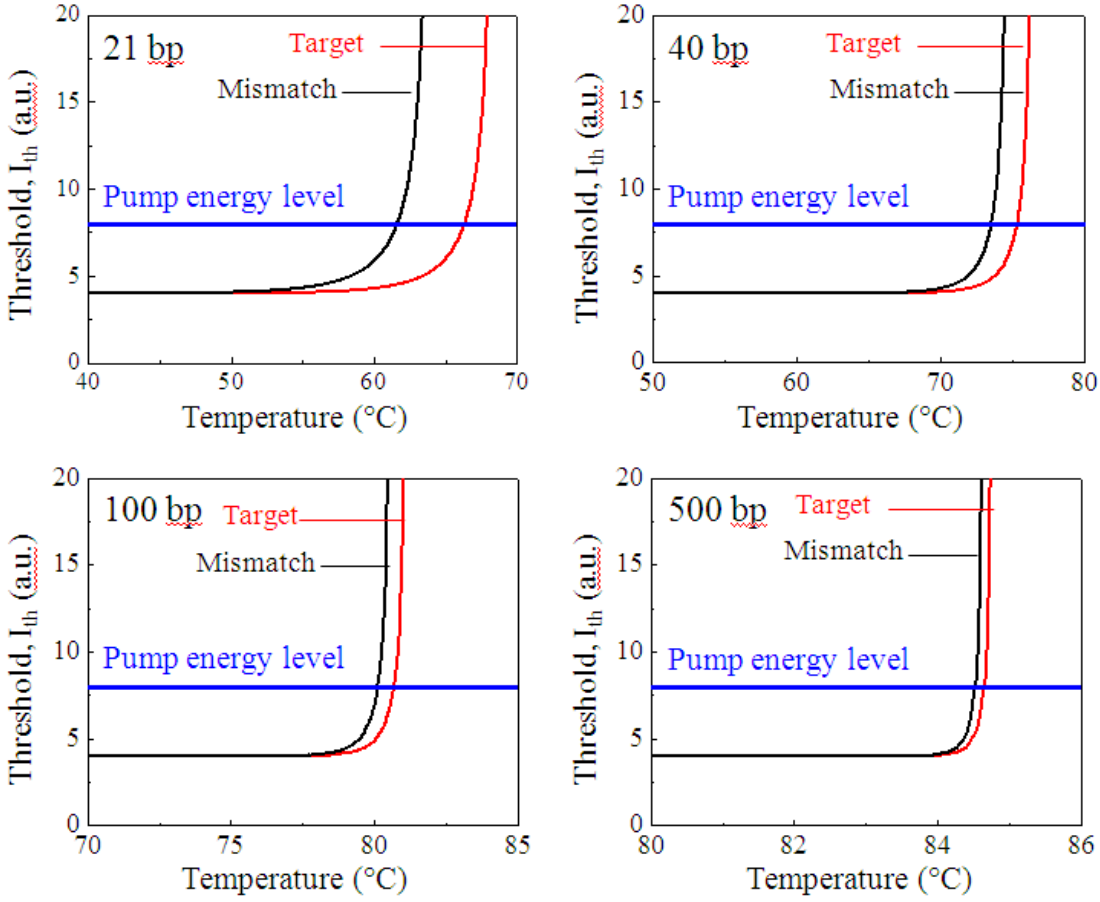

Figure 5.4 Lasing threshold calculated for the target and the single-base-mismatched DNA with 21, 40, 100 and 500 bases. γ is set to be 0.8.

Fig. 5.4 shows the calculated lasing thresholds for the target DNA of 21, 40, 100 and 500 bases long and their single-base-mismatched counterparts, as a function of temperature (see Table 5.1 in for the details of the DNA sequences). At a relatively low temperature, the external pump energy level (I_{pump}) is higher than the corresponding lasing threshold for the target and the mismatched DNA. Consequently, lasing emission should occur for both samples. As temperature increases, the lasing threshold increases rapidly due to decreased Γ. At the temperature where the threshold becomes higher than the given pump energy level, the laser output ceases, indicating a phase transition from lasing emission to regular fluorescence with orders of magnitude change in output intensity. According to Eqs. (5.9)-(5.13), the target DNA always has a slightly higher transition temperature than the mismatched DNA for a given pump energy level, which is shown in Fig. 5.4. In addition, when I_{pump} is sufficiently high, the difference in the transition temperature is independent of I_{pump}, which, in conjunction with the sharp phase transition, allows us to accurately determine the transition temperature difference for clear distinction between the target and the mismatched DNA, as discussed next.

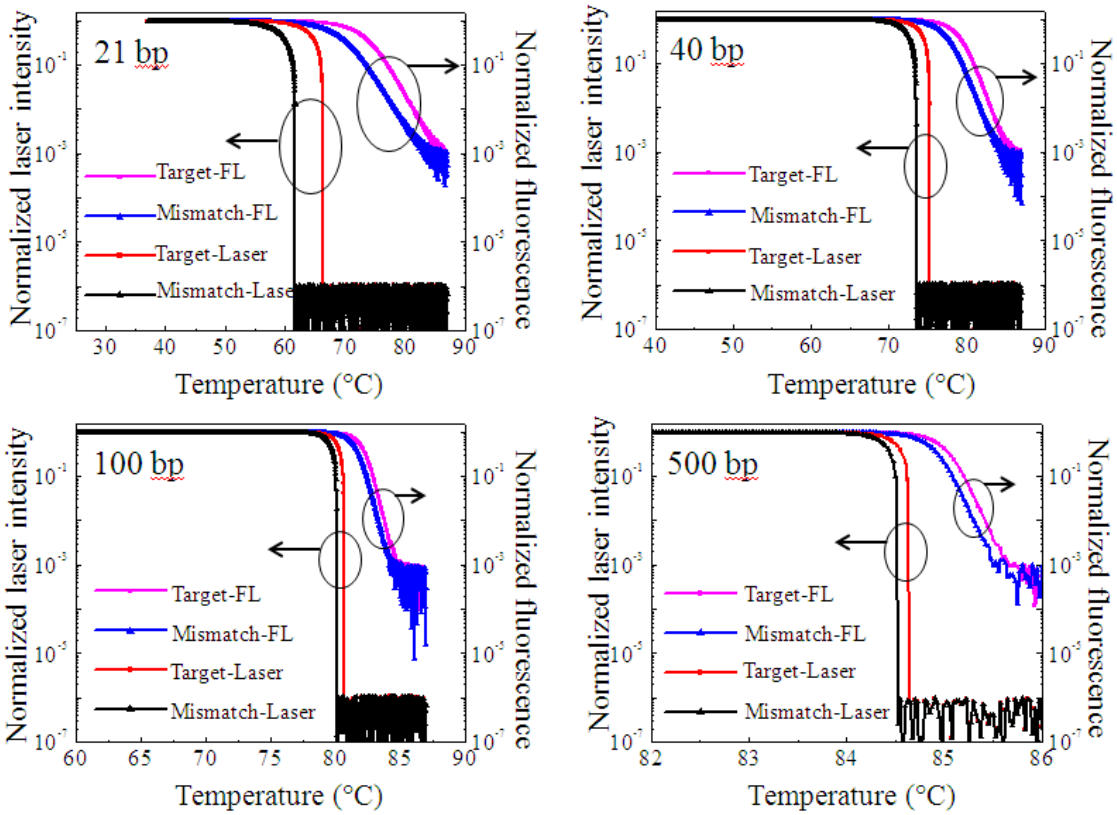

Figure 5.5 Corresponding normalized laser output intensity and fluorescence using eqs 4 and 5. All the DNA sequences are listed in Table 5.1. All curves are normalized to their respective maximal intensity at 23 °C. The laser transition temperature, at which the laser intensity drops to zero, is 75.25 °C and 73.52 °C for the 40 bases long target and the single-base mismatch. the same level of instrument noise is added to both laser output and fluorescence. Note that the relative noise level in the laser output appears to be orders of magnitude lower than that in fluorescence due to the fact that the laser output intensity is much higher than fluorescence.

Fig. 5.5 plots the normalized laser emission and fluorescence emission corresponding to the samples used in Fig. 5.4. As compared to the fluorescence based melting curve, the prevailing feature in the laser emission based melting curve is the sharp phase transition at which the emitted light intensity changes drastically.

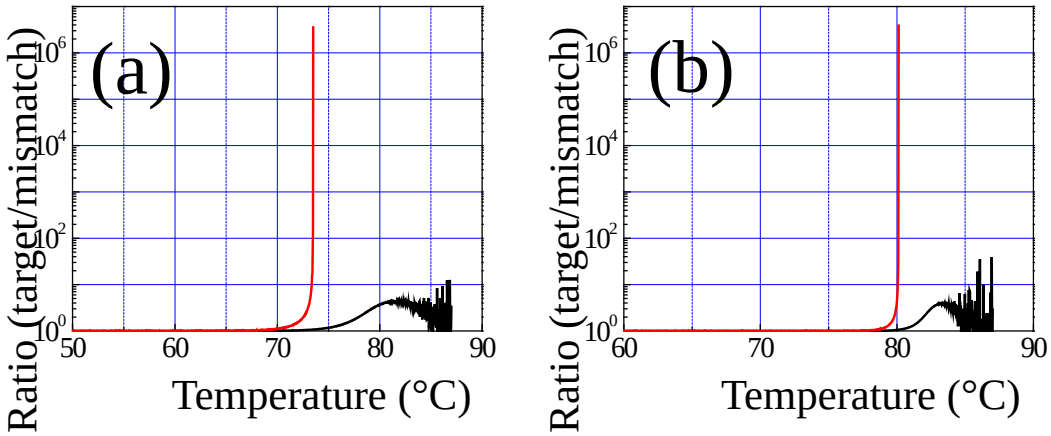

Figure 5.6 Calculated differential ratios of the laser outputs (red curves) and the fluorescence intensities (black curves) from the target and the mismatch: (a) 40-bases-ling DNAs, (b) 100-bases-long DNAs. Note that the ratio for the laser output shows extremely high value near the transition temperature while the ratio for the fluorescence remains under 10 and is deteriorated by embedded noises.

This cut-off behavior provides an extremely high differential signal. The emission ratio between the target and the mismatched DNA is shown in Fig. 5.6. It enables accurate determination of the difference in transition temperature in actual experiments. Based on Fig. 5.4, the transition temperature difference is approximately 1.73 °C obtained with the laser emission, very close to the difference of 1.70 °C in the DNA melting temperature calculated with fluorescence method (DNA melting temperature is defined as the temperature at which the fluorescence drop to 50% of its maximum at a low temperature). Another important feature is that the target and mismatched DNA melting curves with the laser emission exhibit appreciable difference at a lower temperature at which the melting curves from the conventional method are virtually the same, highlighting the underlying optical amplification mechanism of the intra-cavity detection.

To mimic the actual measurement, the same level of noise is added to both laser emission and fluorescence as the instrument noise (such as detector's noise, etc.). Since the laser emission is orders of magnitude stronger than fluorescence, the relative impact of the noise on the laser emission based melting curve (particularly, around the sharp phase transition) becomes negligible. In contrast, the fluorescence based melting curve is much more susceptible to noise, which drastically affects the determination of melting temperature difference and the overall curve shape, especially when (1) longer DNA sequences are to be distinguished (in which case the fluorescence difference becomes smaller) and (2) low sample volumes are used (in which case the fluorescence becomes weaker).

Fig. 5.4 and 5.5 also show the lasing thresholds and the laser/fluorescence intensities corresponding to the target and the single-base-mismatched DNA of 21, 100 and 500 bases long as well. As compared to the 40 bases long DNA, the phase transition for longer DNAs occurs at a higher temperature, as expected. While the transition temperature differences become smaller, the differential remains the same and is not degraded by the noise. It should be emphasized that the theoretical analysis discussed here is very generic and the detection principle is applicable to any optofluidic laser cavities, such as a ring resonator, Fabry-Perot cavity, and distributed feedback laser cavity.

5.4 Materials and methods

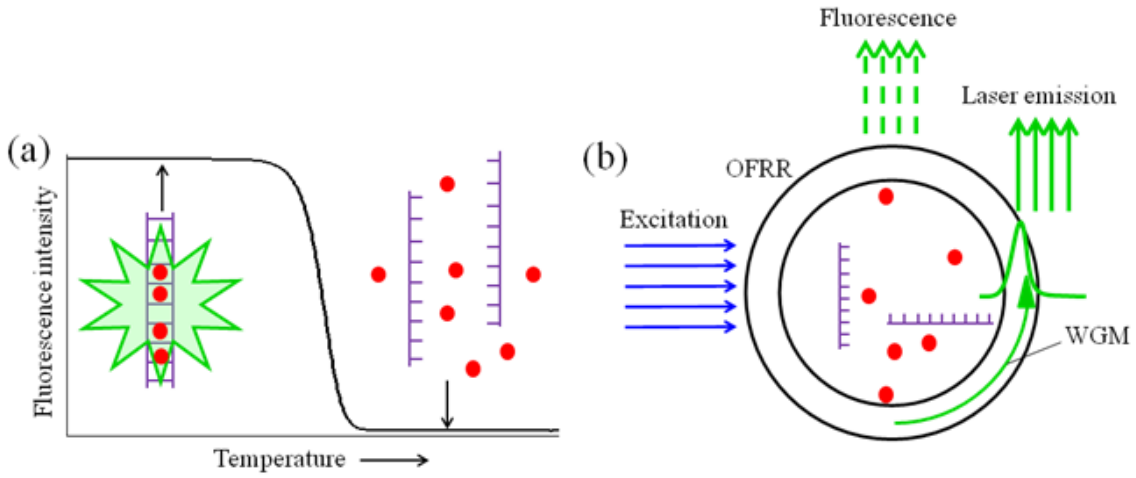

Figure 5.7 (a) DNA melting analysis with the saturation dye. The saturation dye has strong fluorescence in the presence of double-stranded DNAs (dsDNAs). As the temperature increases, dsDNAs melt into single-stranded DNAs. Consequently, fluorescence from the saturation dye diminishes. (b) Schematic of the glass capillary based optofluidic ring resonator (OFRR) laser. The whispering gallery mode (WGM) interacts evanescently with the dye flowing through the capillary and provides the optical feedback for lasing. The laser emission can be collected at the edge of the OFRR, whereas the conventional fluorescence can be collected from the center part of the OFRR, which has no interaction with the WGM.

In this paper, we use the optofluidic ring resonator (OFRR) to demonstrate an intra-cavity DNA melting analysis, as illustrated in Fig. 5.7(b). The OFRR is based on a thin-walled fused silica microcapillary, whose cross-section forms a ring resonator that supports the whispering gallery mode (WGM) circulating along the capillary circumference as explained previously. The WGM interacts evanescently with the sample solution of the DNA and the saturation dye flowing through the OFRR, which provides an optical feedback for the dye to lase. Details of the OFRR fabrication, experimental setup, and sample preparation are described as follows.

5.4.1 Fabrication of the OFRR.

The microcapillary OFRR is fabricated with a pre-etched fused silica capillary preform (Polymicro Technologies, TSP700850) by the conventional drawing method reported previously (7, 29, 62, 93, 115-117). Briefly, the fused silica capillary with an outer diameter and inner diameter of 850 μm and 700 μm, respectively, is wet-etched with 5% hydrofluoric acid for 48 hours and pulled under CO_2 laser radiation. The outer diameter and the wall thickness of the microcapillary after the pulling process are 80 μm and 5 μm, respectively.

5.4.2 Sample preparation.

The linearly structured DNA sequences used in the experiments (the target DNA and the single-base-mismatched DNA with 21, 40, and 100 bases long) are given in Table 5.1. SYTO 13® nucleic acid stain (Invitrogen, originally dissolved in DMSO with 5 mM concentration) is used as the saturation dye, and is separately mixed to the target and the mismatch samples. The mixture of DNA and the saturation dye is dissolved in the buffer solution (TRIS-acetate-EDTA buffer, pH = 8.3) with the final concentration of 250 μM for both DNAs and the saturation dye.

5.4.3 Experimental setup.

The OFRR is pumped with an optical parametric oscillator (Continuum, 5 ns pulsed laser, wavelength = 488 nm, repetition rate = 20 Hz) while the fused silica capillary is being filled with the sample solution. The external light source is focused onto the OFRR part of the microcapillary with a spot size of 3.8 mm^2, and the pump

energy density is controlled by a neutral density filter. The laser signal and the fluorescence emission free-space-coupled into the multi-mode fiber are measured by the spectrometer (HR550i, Horiba Jobin Yvon) simultaneously.

5.5 Results and discussion

5.5.1 Laser emission spectra

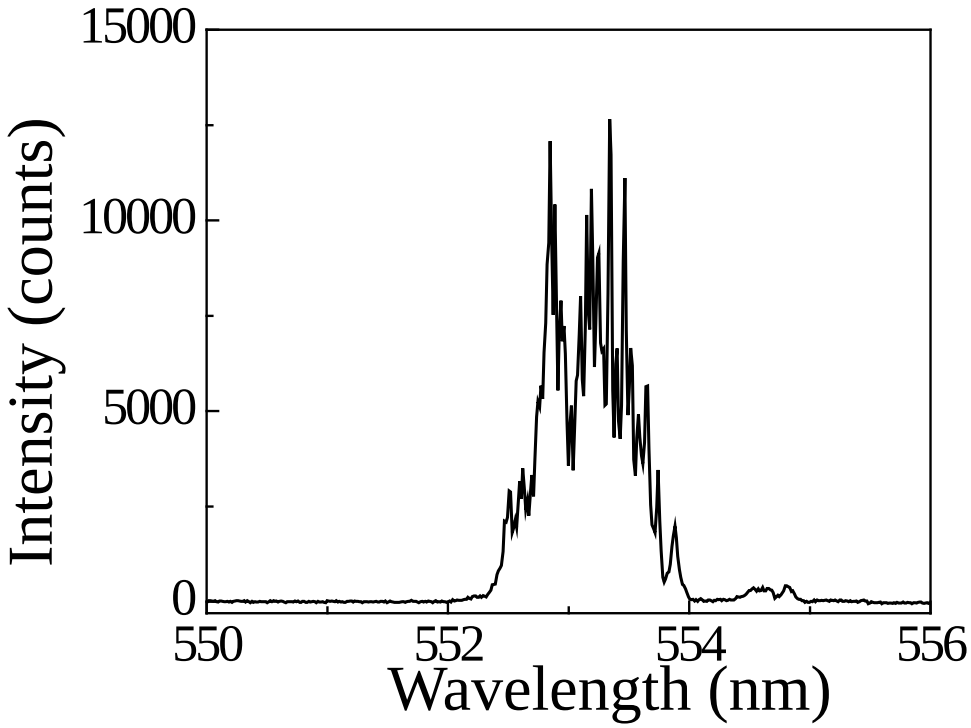

Figure 5.8 Signature multi-mode lasing emission spectrum for our OFRR based DNA laser. The sample solution containing 40-bases-long target DNAs and the saturation dye with the concentration of both 250 μM is optically pumped inside of the capillary OFRR. The pump energy density is 0.98 mJ/mm^2.

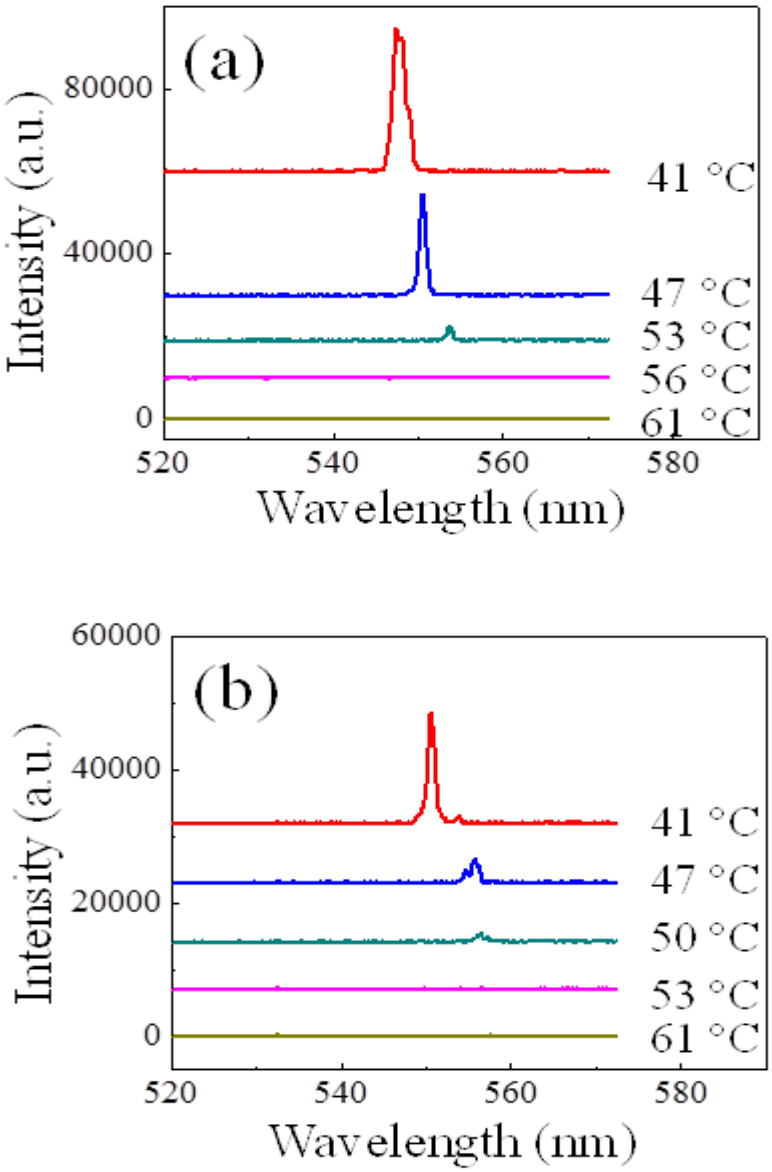

Figure 5.9 Examples of the lasing spectra for (a) the target DNA and (b) the single-base-mismatched DNA with 40 bases above and below their respective laser transition temperature. The concentration of the DNA and the saturation dye are both 250 μM. The pump energy density is 980 μJ/mm^2 per pulse. Curves are vertically shifted for clarity. The DNA sequences are listed in Table 5.1.

Figure 5.8 and 5.9 present the laser emission spectra from the 40 bases long target and the corresponding single-base-mismatched DNA at various temperatures. At low

temperature, all samples show the signature multi-mode lasing emission peaks as in Fig. 5.8 for a higher resolution laser spectrum. With increased temperature, the laser intensity for both the target and the mismatched DNA decreases and eventually disappears, indicating a phase transition from laser emission to fluorescence. However, the transition temperature for the target is higher than that for the mismatched DNA. For example, the laser emission from the target DNA still persists at 53°C (see Fig. 5.9(a)), whereas the mismatched DNA shows virtually no lasing signal (see Fig. 5.9(b)).

5.5.2 Signal intensity vs temperature

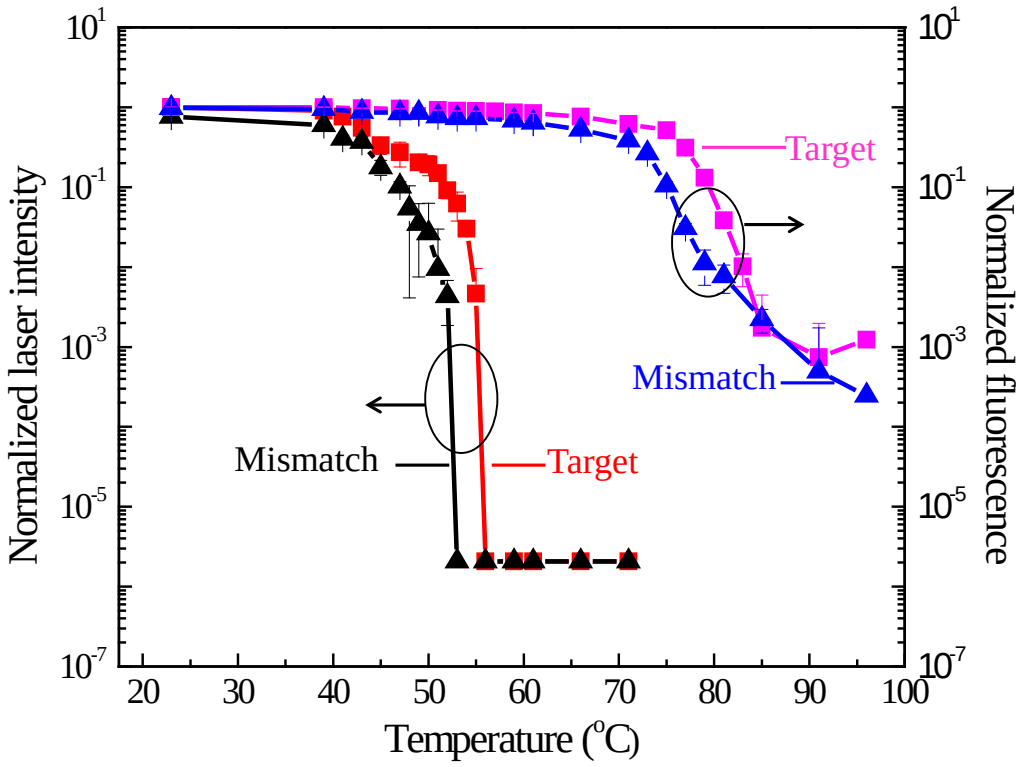

Figure 5.10 Spectrally integrated lasing intensity for the target and the single-base-mismatched DNA as a function of temperature obtained from Fig. 3 with finer temperature increment. The lasing transition, at which point the laser signal disappears, occurs at approximately 56°C and 53°C for the target and the single-base-mismatched DNA, respectively. For comparison, conventional fluorescence signals that are acquired concomitantly with the laser signals are also plotted. All curves are normalized to the respective target intensity at temperature of 23°C. Error bars are obtained by 5 measurements.

Fig. 5.10 shows the OFRR laser based DNA melting curves extracted from the spectra in Fig. 5.9 with a finer temperature increment. Meanwhile, the fluorescence based DNA melting curves are also obtained simultaneously under otherwise the same conditions. Overall, both the laser emission and the fluorescence curves agree

qualitatively with the respective theoretical predictions. For the fluorescence based melting curves, the melting temperature of the target and the mismatched DNA is 72 °C and 68 °C, respectively, which is further verified by a commercial DNA melting analysis instrument (Chromo4TM CFB-3240G, Bio-rad). In contrast, the laser emission exhibits a very sharp transition, with the transition temperature difference of approximately 4 °C. The maximal differential signal is over 10^4 around 53 °C for intra-cavity detection, whereas the differential signal is approximately 10 at best and only 1.4 at the melting temperature (68 °C) for the conventional detection. Furthermore, the relative noise level is dramatically reduced for the laser due to its orders-of-magnitude higher signal intensity.

Fig. 5.11 shows the differential signal extracted from Fig. 5.10, which agrees qualitatively with the theoretical analysis in previous chapter.

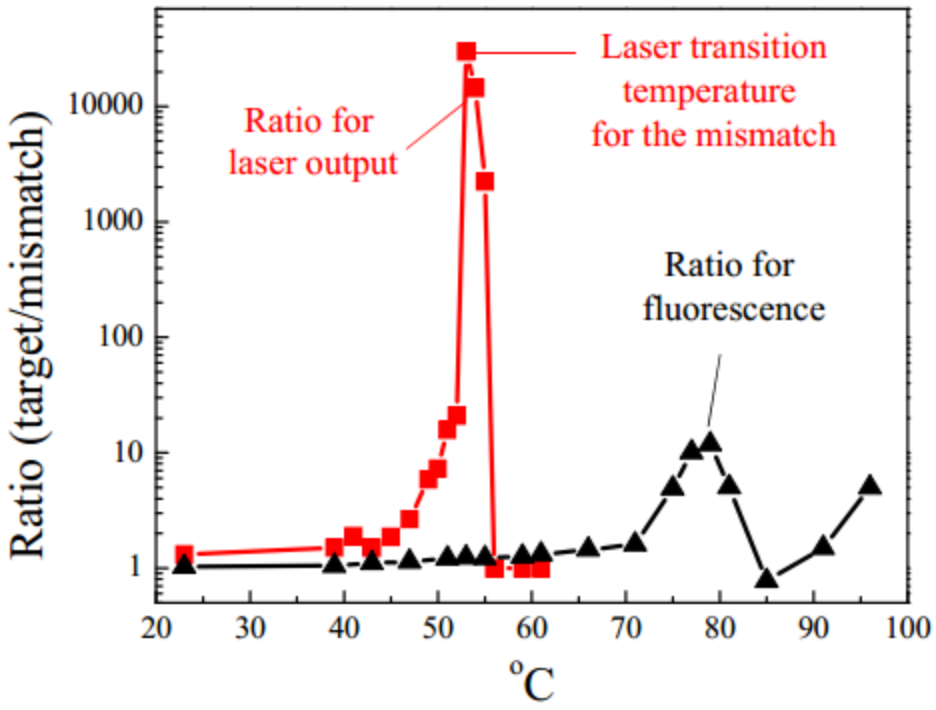

Figure 5.11 Differential signal for laser output (red curve) and fluorescence intensity (black curve) extracted from Fig. 5.10.

5.5.3 Signal intensity vs pump energy density

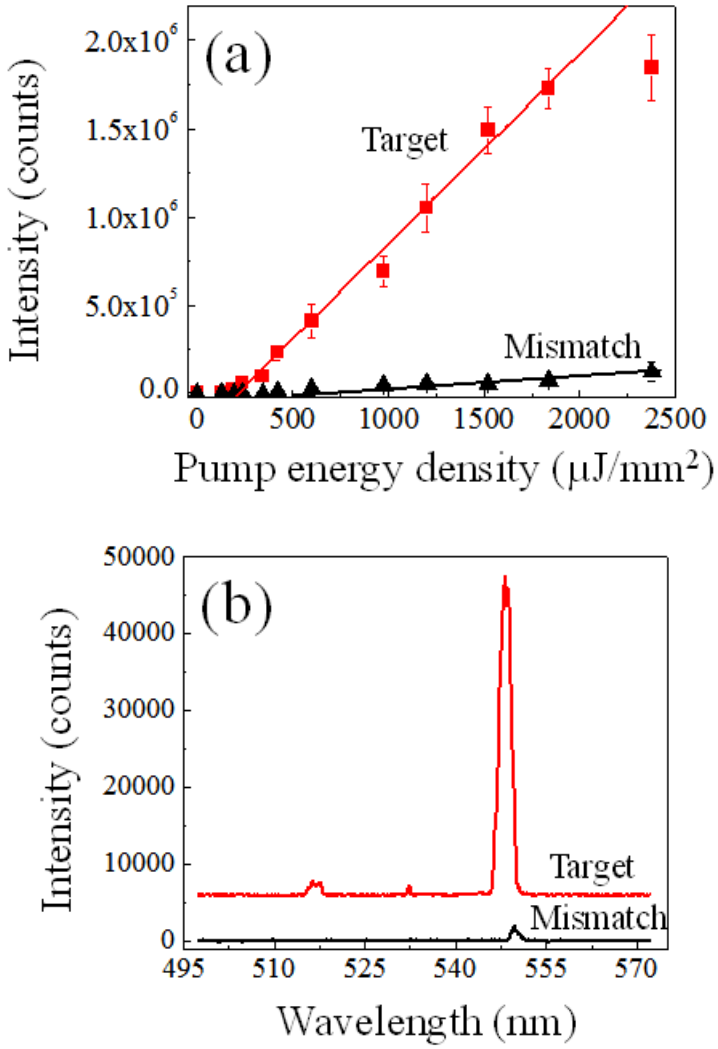

Figure 5.12 (a) Spectrally integrated lasing intensity as a function of pump energy density for the target and the single-base-mismatched DNA listed in Table 5.1, when the temperature is fixed to 51 °C. The signal from the target DNA has a lasing threshold of approximately 216 μJ/mm^2 and shows typical lasing characteristics with a high lasing efficiency. The signal from the mismatch has a lasing threshold of approximately 500 μJ/mm^2 and shows only small lasing signal, even at high pump intensities. Solid lines are the linear fit above the threshold. (b) Representative lasing spectra at 51°C for the target and the mismatch when the pump intensity is 1.84 mJ/mm^2. The integrated lasing intensity of the target DNA shows approximately 25 times higher than that of the single-base-mismatched DNA. The curves are vertically shifted for clarity. Error bars are obtained by 5 measurements.

Once the transition temperature is determined for a given target and its corresponding mismatch, the DNA can also be differentiated by scanning the excitation energy while keeping the temperature constant. Fig. 5(a) presents the spectrally integrated laser intensities for the same target and mismatched DNA used in Figs. 3 and 4 when temperature is fixed at 51 °C. The target shows a clear laser characteristic with a lasing threshold of 216 μJ/mm^2 and high lasing efficiency of 1100 per μJ/mm^2, while the mismatch has a much higher lasing threshold of 500 μJ/mm2 with lasing efficiency of only 70 per μJ/mm^2. Due to such large difference between the signal from the target and the mismatch, it may be even possible to distinguish the target from the mismatch without scanning the pump at all. This is exemplified by Fig. 5.12(b) where the pump energy density is 1.84 mJ/mm^2. The integrated laser intensity for the target is approximately 25 times higher than for the mismatch. Such large difference can only be obtained with the optical amplification. For comparison, the difference between the target and the mismatched DNA is only 10% at same temperature for the conventional fluorescence detection, according to Fig. 4. Note that the clearly distinguishable optical signal can be obtained with only one laser pulse excitation, which makes DNA detection much faster and simpler. In particular, for shorter DNA sequences, the DNA can even be distinguished at room temperature with the laser emission (see Fig. 5.13.), while conventional melting curve analysis shows virtually no discrimination isothermally. (see Fig. 5.14.)

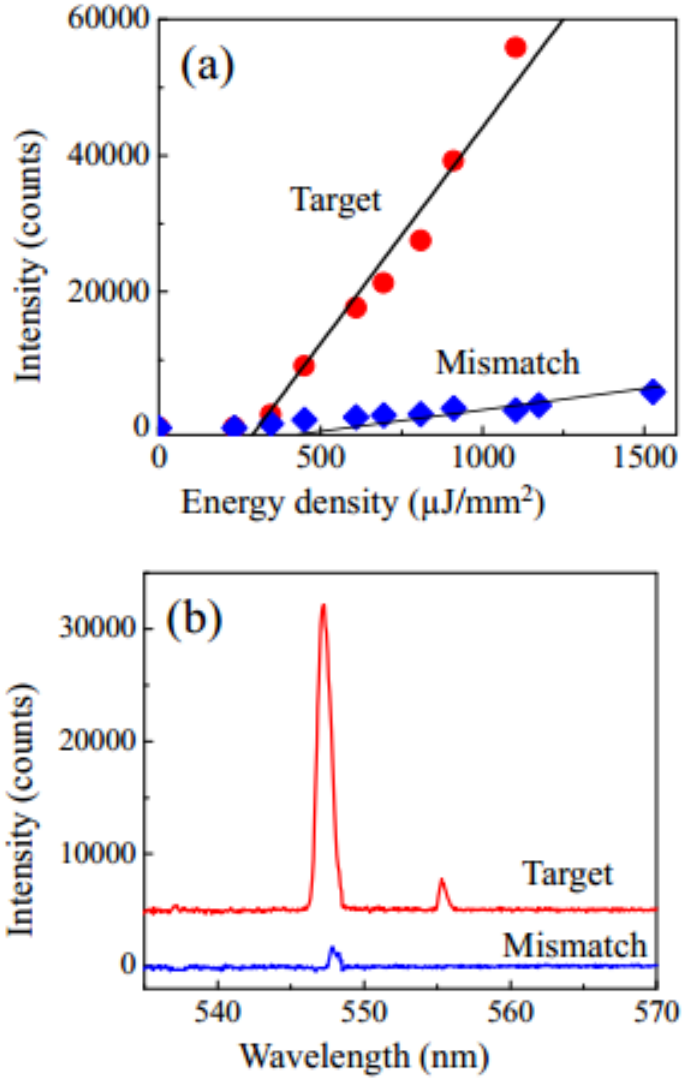

Figure 5.13 (a) Spectrally integrated lasing intensity as a function of pump energy density for the target and the single-base-mismatched DNA of 21 bases long at room temperature. The signal from the target has a lasing threshold of approximately 305 μJ/mm^2 and shows typical lasing characteristics with a high lasing efficiency. The mismatch shows only small lasing signal, even at high pump intensities. (b) Representative lasing spectra for the target and the mismatch when the pump intensity is 809 μJ/mm^2. The integrated lasing intensity of the target shows 21.4 times higher than that of the mismatch. The curves are vertically shifted for clarity.

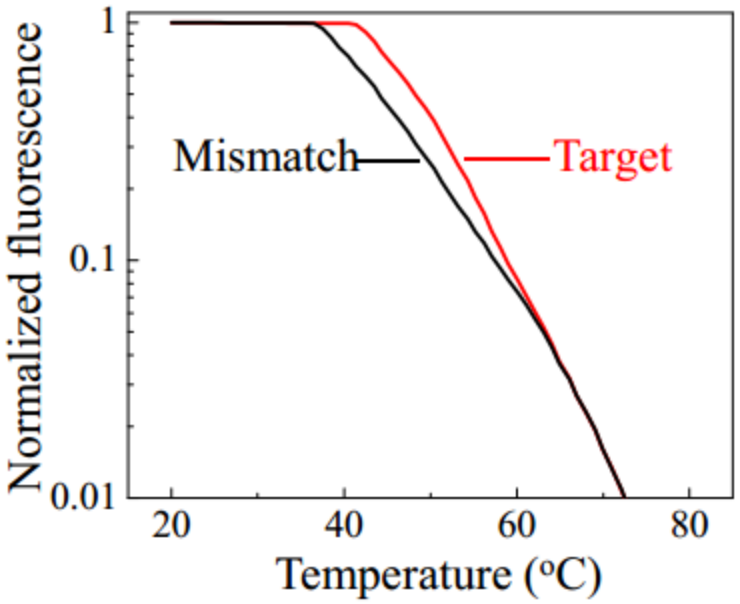

Figure 5.14 Standard melting curve analysis for 21 bases long DNAs obtained with Chromo4TM CFB-3240G (Bio-rad). Note that the target and the mismatch show virtually identical fluorescence at room temperature. The details of the DNA samples are given in Table 5.1.

5.5.4 100 bases long DNA sequences

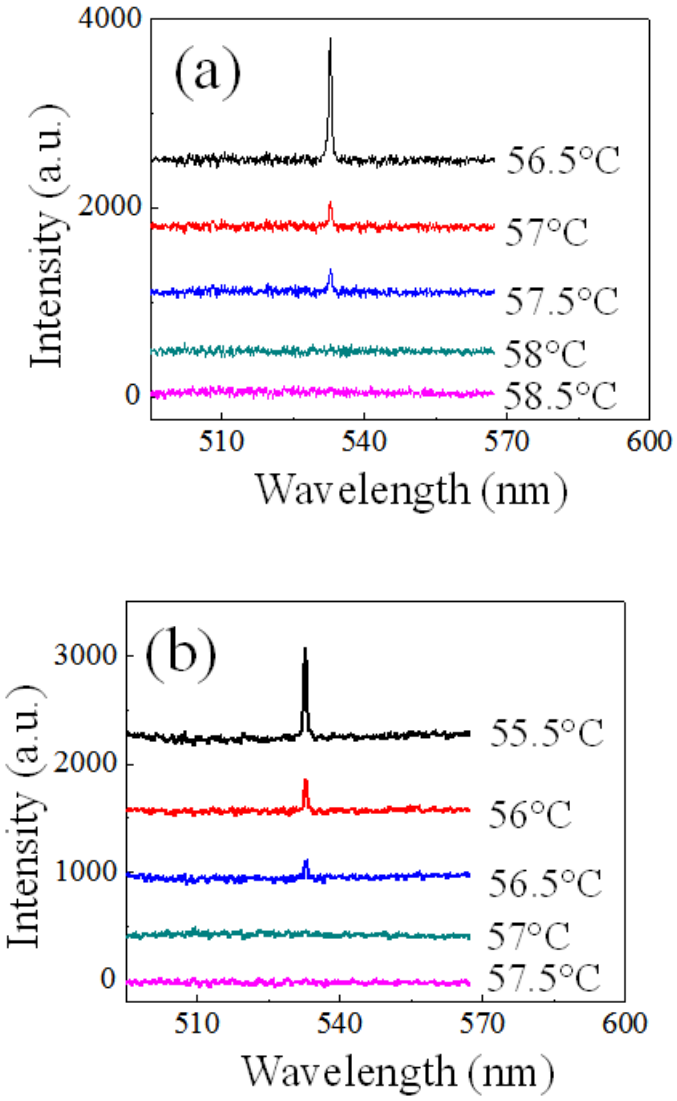

Figure 5.15 Lasing spectra for (a) the target DNA and (b) the single-base-mismatched DNA with 100 bases above and below their respective laser transition temperature. Note that the two samples show the transition temperature difference of approximately 1°C. The concentration of the DNAs and the saturation dye are 250 μM. The pump energy density is 0.8 mJ/mm^2 per pulse. Curves are shifted vertically. The DNA sequences are listed in Table 5.1.

We now move to validate the intra-cavity detection principles with longer DNA sequences. Fig. 5.15 illustrates the lasing spectra for the target DNA and the single-base-

mismatched DNA with 100 bases long when the pump energy density is fixed at 0.8 mJ/mm^2. The melting curves show very similar temperature dependence in comparison with the previous results using 40 bases long DNAs. The transition temperature of the target and the mismatch is increased to 57.5°C and 56.5°C, respectively. Although the transition temperature difference decreases to 1°C, the target and the mismatched DNA can still be clearly distinguished by the cut-off phase transition behavior at 57.5°C and 56.5°C.

5.6 Conclusion

In conclusion, we have achieved lasing from the saturation dye and the DNA mixture, which can be utilized to differentiate the target DNA and the base-mismatch. The target and the mismatch show clearly distinguishable lasing characteristics, thus enabling rapid and selective detection of the mismatch. The novel detection method does not require complexity such as labeling, and is a highly competitive technology in mutation scanning for medical diagnosis and biological researches.

As a lasing activity from the saturation dye in the presence of dsDNA, we uncover possibilities of the OFRR laser as the DNA detecting scheme. Our next goal is to discriminate longer DNA sequences from mismatches through modification of temperature. The future work will focus on further study of this detection system relying on OFRR lasers. The realized system will have several advantages over existing genotyping methods: (1) Direct, rapid detection of the DNA can be achieved. Once the condition is obtained, each sample can be analyzed with a single shot of laser, which takes a few milliseconds. (2) Thanks to the nature of the laser, we can achieve significant difference in the signal intensity between the target and the mismatch, compare to fluorescence-based methods. (3) Refer to our droplet laser work, the OFRR laser can be achieved with the sample volume of down to a few nLs. The concentration of DNA/saturation dye we use (150 μM) associated with ~1 nL sample volume gives about 10^{11} copies. For the HRM, typically uses sample volume of 50 μL with the DNA concentration of a few μM, approximately 10^{14} copies of PCR amplicons are used in a single analysis. 10^3 times difference gives a reduction of 10 PCR cycles. (4) Lasing signal difference occurs in the lower temperature compare to fluorescence. Since the analyzing

time is also extremely short, less amount of heating is applied to the sample, which is favorable for most biological detecting study. (5) Connecting to upstream/downstream optofluidic channel, the detection using the OFRR laser can be operated with not only a perishable bio-sample but also living cells/tissues. If the amount of DNA sequences is abundant, our system does not require PCR prior to the detecting procedure.

Chapter VI

Summary and Suggestions for Future Work

In previous chapters, novel optofluidic ring resonator (OFRR) laser schemes resolving problems of existing OFRR lasers are suggested and DNA melting analysis utilizing the OFRR laser is demonstrated. A PDMS-based OFRR laser using two optically coupled ring resonators in different sizes has addressed an intrinsic multi-mode emission of ring resonator laser. The single-wavelength lasing by Vernier effect can be tuned by modification of refractive index of the gain medium as well. A micro-bubble filled with liquid gain medium mimics the droplets in air that have 3-dimensional optical confinement. The quasi-droplet laser based on the micro-bubble shows superior lasing characteristics due to its sub-micron thin wall and enables repetitive interrogation and easy directional laser emission out-coupling without evaporation or size/shape variations. A microdroplet is delivered to the capillary OFRR downstream and a laser emission, which can be conveniently coupled into an optical fiber, is achieved. An efficient FRET lasing is also demonstrated making the microdroplet an attractive reaction chamber with small sample volume. Furthermore, an intracavity DNA melting analysis dramatically improves discrimination of optical signals. The laser amplifies thermodynamic difference in between the target DNA and the base-mismatched DNA. The OFRR laser based detection leads to novel optofluidic devices that enable rapid and simple analysis of DNA sequences.

6.1 Self-assembled DNA tetrahedral optofluidic lasers

The OFRR lasers developed in this thesis are optically pumped dye-specific lasers, which has laser emission determined by dye molecules not by laser cavities. Thus, they should be pumped with wavelength tunable light sources according to the dye absorption and emission. In most cases, a variation of the external light sources is limited, requiring multiple lasing emissions from a single pump laser wavelength. In chapter 5, I demonstrated a FRET laser using microdroplets for those purpose, however it requires relatively high dye molecule concentration due to short energy transfer radius between the donor and the acceptor molecules.

DNA has unparalleled ability of programmable hybridization through unique base pair recognition and is a very powerful material for bottom-up nanofabrication. Indeed, DNA nanostructures offer versatile ways for the anchoring of (bio)molecules and nanoparticles with high addressability and a nanoscale resolution of 6 nm. Sun et al. demonstrated nice works on optofluidic dye laser utilizing FRET via DNA scaffolds, in which the donor and acceptor are conjugated with DNA sequences with the predetermined donor-to-acceptor distance, ratio, and spatial configuration.(93) Likewise, DNA tetrahedral provides an ideal platform for the precise anchoring of dye molecules for laser applications. The DNA tetrahedral consists of a FRET pair can precisely control the laser characteristics of the OFRR laser and reduce required dye concentration for lasing as well.

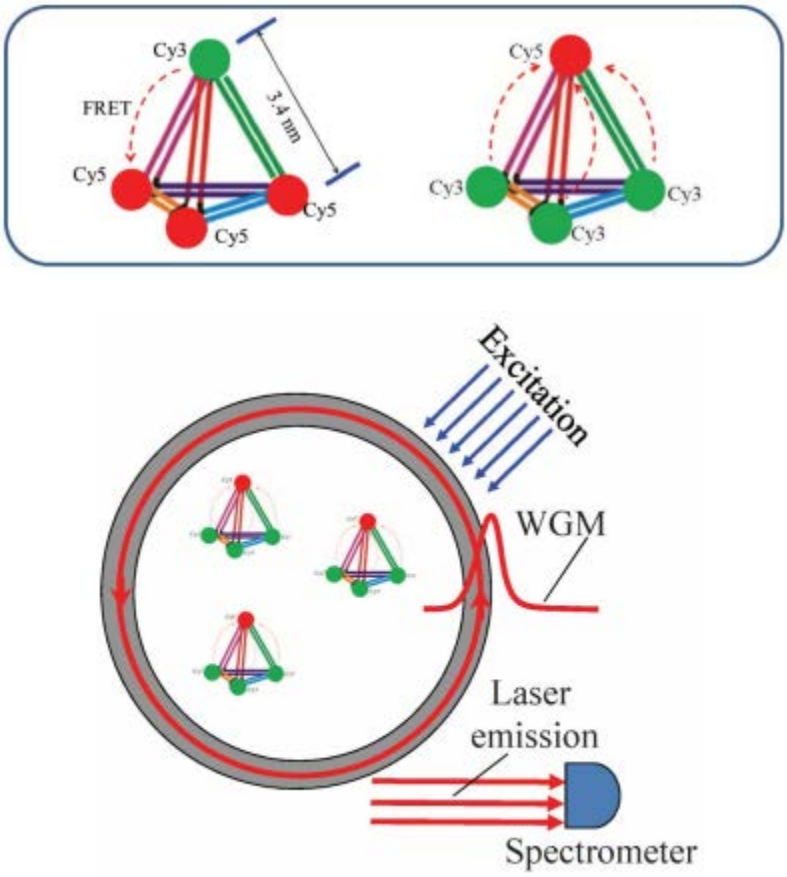

Figure 6.1 Concept of DNA tetrahedral FRET laser.

A laser gain is one of the most important parameters, which determines many other laser characteristics such as lasing threshold, efficiency and output power. As illustrated in Fig. 6.1, the gain medium of the optofluidic laser consisted of a fluorescence resonance energy transfer (FRET) pair, Cy3 (donor) and Cy5 (acceptor), is attached to the vertex of the DNA tetrahedron. Cy3 acts as an antenna to collect the excitation light and then transfers the energy through FRET for Cy5 to lase.

In the future, the optofluidic laser consisted of the DNA tetrahedron will further be investigated. Optimization of the Cy3 and Cy5 arrangement on the DNA tetrahedron will result in a significant improvement in the lasing characteristics such as the lasing

threshold, the lasing efficiency and most of all, the molecular concentration. A theoretical analysis will be also carried out to elucidate the control and tuning capability of the DNA nanostructures. The combination of the aforementioned biological nanoengineering concept and the optofluidic laser takes advantage of the self-recognition and self-assembly capabilities of biomolecules with sub-nanometer accuracy, their well-defined structures and stoichiometry, thus enabling the precise control and tuning of the laser characteristics at the molecular level.

6.2 Optofluidic ring resonator laser with surface gain medium

In chapter 4, microdroplets are utilized as a reaction chamber in nL size revealing possibilities of the optofluidic laser in practical applications for bio/chemical sensing. In realistic cases, not only volume of the biological sample but also a concentration of molecules in interest can be limited. As mentioned previously, the OFRR laser requires relatively high dye molecular concentration to its extremely high Q-factor optical cavity. Since the OFRR laser to date relies on the evanescent field near the ring resonator surface, only a small fraction of the gain medium involves in the optical gain. On the other hand, laser schemes other than the OFRR such as Fabry-Perot cavity laser use most of sample volume for optical feedback, while they have difficulties in achieving Q-factors comparable to that of the OFRR.

The FRET laser based on DNA scaffolds leads to an idea that the dye molecules can be concentrated on the surface of the OFRR with immobilized DNA probes. In that case, even a biological sample with limited concentration can achieve enough optical gain for laser through the OFRR surface. With the DNA probe labeled with donor molecule, a simply switchable OFRR laser with a single-wavelength pump can be demonstrated, since the gain medium in the surface can easily be replaced by controlling double-strand binding of the DNA scaffolds. Researches in the future may include such approaches for decreasing dye molecular concentrations of the OFRR lasers, not only from improving already high optical Q-factor of the cavities.

BIBLIOGRAPHY

1. Psaltis D, Quake SR, & Yang C (2006) Developing optofluidic technology through the fusion of microfluidics and optics. *Nature* 442:381-386.
2. Fainman Y, Lee LP, Psaltis D, & Yang C (2009) *Optofluidics: Fundamentals, Devices, and Applications* (McGraw Hill, New York, NY).
3. Hawkins AR & Schmidt H (2010) *Handbook of Optofluidics* (CRC Press, Boca Raton, FL).
4. Monat C, Domachuk P, & Eggleton BJ (2007) Integrated optofluidics: a new river of light. *Nat. Photonics* 1:106-114.
5. Tibbe AGJ, Miller MC, & Terstappen LWMM (2007) Statistical considerations for enumeration of circulating tumor cells. *Cytometry, Part A* 71A(3):154-162.
6. Li Z & Psaltis D (2008) Optofluidic dye lasers. *Microfluid. Nanofluid.* 4:145–158.
7. Shopova SI, Zhu H, & Fan X (2007) Optofluidic ring resonator based dye laser. *Appl. Phys. Lett.* 90:221101.
8. Helbo B, Kristensen A, & Menon A (2003) A micro-cavity fluidic dye laser. *J. Micromech. Microeng.* 13:307-311.
9. Vannahme C, Christiansen MB, Mappes T, & Kristensen A (2010) Optofluidic dye laser in a foil. *Opt. Express* 18:9280-9285.
10. Li ZY, Zhang ZY, Emery T, Scherer A, & Psaltis D (2006) Single mode optofluidic distributed feedback dye laser. *Opt. Express* 14:696-701.
11. Song W, Vasdekis AE, Li Z, & Psaltis D (2009) Low-order distributed feedback optofluidic dye laser with reduced threshold. *Appl. Phys. Lett.* 94:051117.
12. Chen Y, Li Z, Zhang Z, Psaltis D, & Scherer A (2007) Nanoimprinted circular grating distributed feedback dye laser. *Appl. Phys. Lett.* 91:051109.
13. Song W, Vasdekis AE, Li Z, & Psaltis D (2009) Optofluidic evanescent dye laser based on a distributed feedback circular grating. *Appl. Phys. Lett.* 94:161110.
14. Scheuer J, Green WMJ, DeRose GA, & Yariv A (2005) InGaAsP annular Bragg lasers: theory, applications, and modal properties. *IEEE J. Quantum Elect.* 11:476-484.
15. Vezenov DV, *et al.* (2005) A low-threshold, high-efficiency microfluidic waveguide laser. *J. Am. Chem. Soc.* 127:8952-8953.

16. Balslev S & Kristensen A (2005) Microfluidic single-mode laser using high-order Bragg grating and antiguiding segments. *Opt. Express* 13:344-351.
17. Kou Q, Yesilyurt I, & Chen Y (2006) Collinear dual-color laser emission from a microfluidic dye laser. *Appl. Phys. Lett.* 88:091101.
18. Song W & Psaltis D (2010) Pneumatically tunable optofluidic dye laser. *Appl. Phys. Lett.* 96:081101.
19. Aubry G, *et al.* (2011) A multicolor microfluidic droplet dye laser with single mode emission. *Appl. Phys. Lett.* 98:111111.
20. Chang RK & Campillo AJ (1996) *Optical Processes in Microcavities* (World Scientific, Singapore).
21. Vahala KJ (2003) Optical microcavities. *Nature* 424:839-846.
22. Sun Y & Fan X (2011) Optical ring resonators for biochemical and chemical sensing. *Analytical and Bioanalytical Chemistry* 399:205-211.
23. Zuta Y, Goykhman I, Desiatov B, & Levy U (2010) On-chip switching of a silicon nitride micro-ring resonator based on digital microfluidics platform. *Opt. Express* 18:24762-24769.
24. Li H, Guo Y, Sun Y, Reddy K, & Fan X (2010) Analysis of single nanoparticle detection by using 3-dimensionally confined optofluidic ring resonators. *Opt. Express* 18(24):25081-25088.
25. Little BE, Laine J-P, & Haus HA (1999) Analytic Theory of Coupling from Tapered Fibers and Half-Blocks into Microsphere Resonators. *J. Lightwave Technol.* 17(4).
26. Manor R, *et al.* (2003) Microfabrication and characterization of liquid core waveguide glass channels coated with Teflon AF. *IEEE Sens. J.* 3:687-692.
27. Memisevic J, Korampally V, Gangopadhyay S, & Grant SA (2009) Characterization of a novel ultra-low refractive index material for biosensor application. *Sens. Actuators B-Chem.* 141:227-232.
28. Morand A, Phan-Huy K, Desieres Y, & Benech P (2004) Analytical Study of the Microdisk's Resonant Modes Coupling With a Waveguide Based on the Perturbation Theory. *J. Lightwave Technol.* 22(3).

29. White IM, Oveys H, & Fan X (2006) Liquid-core optical ring-resonator sensors. *Opt. Lett.* 31(9):1319-1321.
30. White IM, Oveys H, Fan X, Smith TL, & Zhang J (2006) Integrated multiplexed biosensors based on liquid core optical ring resonators and antiresonant reflecting optical waveguides. *Appl. Phys. Lett.* 89:191106.
31. Li Z, Zhang Z, Scherer A, & Psaltis D (2007) Optofluidic microring dye laser. *IEEE/LEOS Summer Topical Meeting*, (IEEE), pp 70-71.
32. Wu X, Sun Y, Suter JD, & Fan X (2009) Single mode coupled optofluidic ring resonator dye lasers. *Appl. Phys. Lett.* 94:241109.
33. Lee W, *et al.* (2011) Tunable single mode lasing from an on-chip optofluidic ring resonator laser. *Appl. Phys. Lett.* 98:061103.
34. Chao C-Y & Guo LJ (2004) Reduction of Surface Scattering Loss in Polymer Microrings Using Thermal-Reflow Technique. *IEEE Photonics Technology Letters* 16(6):1498-1500.
35. Chen J, Wang W, Fang J, & Varahramyan K (2004) Variable-focusing microlens with microfluidic chip. *J. Micromech. Microeng.* 14:675-680.
36. Chern GD, *et al.* (2003) Unidirectional lasing from InGaN multiple-quantum-well spiral-shaped micropillars. *Appl. Phys. Lett.* 83(9):1710-1712.
37. Luo X & Poon AW (2007) Coupled spiral-shaped microdisk resonators with non-evanescent asymemetric inter-cavity coupling. *Opt. Express* 15(25):17313-17322.
38. Poon AW, Luo X, Chen H, Fernandes GE, & Chang RK (2008) Microspiral resonators for integrated photonics. *Opt. Photonics News* 19:48-53.
39. Ryu J-W, Lee S-Y, & Kim SW (2009) Coupled nonidentical microdisks: Avoided crossing of energy levels and unidirectional far-field emission. *Phys. Rev. A* 79:053858.
40. Trivedi V, Doshi A, Kurup G, & Ereifej E (2010) A modular approach for the generation, storage, mixing, and detection of droplet libraries for high throughput screening. *Lab. Chip* 10(18):2433-2442.
41. Tzeng H-M, Wall KF, Long MB, & Chang RK (1984) Laser emission from individual droplets at wavelengths corresponding to morphology-dependent resonances. *Opt. Lett.* 9:499-501.

42. Haynie DT (2001) *Biological Thermodynamics* (Cambridge University Press).
43. Smith JM, Ness HCV, & Abbott MM (2005) *Introduction to Chemical Engineering Thermodynamics* (McGraw Hill).
44. Kelley SO, Boon EM, Barton JK, Jackson NM, & Hill MG (1999) Single-base mismatch detection based on charge transduction through DNA. *Nucleic Acids Research* 27(24):4830–4837.
45. Zeglis BM & Barton JK (2007) DNA base mismatch detection with bulky rhodium intercalators: synthesis and applications. *Nature Protocols* 2(2):357-371.
46. Sosnowski RG, Tu E, Butler WF, O'Connell JP, & Heller MJ (1997) Rapid determination of single base mismatch mutations in DNA hybrids by direct electric field control. *Proc. Natl. Acad. Sci. USA* 94:1119–1123.
47. Chen Z, *et al.* (2012) Label-free detection of target DNA sequence and single-base mismatch in hepatitis C virus corresponding to oligonucleotide by resonance light scattering technique. *RSC Advances* 2:2562–2567.
48. Jones PA & Baylin SB (2002) The fundamental role of epigenetic events in cancer. *Nature Rev. Genet.* 3:415-428.
49. Wang DG, *et al.* (1998) Large-Scale Identification, Mapping, and Genotyping of Single-Nucleotide Polymorphisms in the Human Genome. *Science* 280:1077-1082.
50. Christopoulos TK (1999) Nucleic acid analysis. *Anal. Chem.* 71:425-438.
51. Sassolas A, Leca-Bouvier BD, & Blum LJ (2008) DNA Biosensors and Microarrays. *Chem. Rev.* 108:109-139.
52. Marras SA, Kramer FR, & Tyagi S (2003) Genotyping SNPs with molecular beacons. *Methods Mol Bio.* 212:111-128.
53. Howell WM, Jobs M, Gyllensten U, & Brookes AJ (1999) Dynamic allele-specific hybridization. *Nature Biotech.* 17:87-88.
54. Tyagi S & Kramer FR (1996) Molecular Beacons: Probes that fluorescence upon hybridization. *Nature Biotech.* 14:303-308.
55. Pease AC, *et al.* (1994) Light-generated oligonucleotide arrays for rapid DNA sequence analysis. *Proc. Natl. Acad. Sci. USA* 91:5022-5026.

56. Ririe KM, Rasmussen RP, & Wittwer CT (1997) Product differentiation by analysis of DNA melting curves during the polymerase chain reaction. *Anal. Biochem.* 245:154-160.

57. Wittwer CT, Reed GH, Gundry CN, Vandersteen JG, & Pryor RJ (2003) High-Resolution Genotyping by Amplicon Melting Analysis Using LCGreen. *Clinical Chemistry* 49(6):853-860.

58. Monis PT, Giglio S, & Saint CP (2005) Comparison of SYTO9 and SYBR Green I for real-time polymerase chain reaction and investigation of the eVect of dye concentration on ampliWcation and DNA melting curve analysis. *Anal. Biochem.* 340:24-34.

59. R.H. LD, Fijnvandraat AC, Ruijter JM, & Moorman AF (2003) Sensitivity and accuracy of quantitative real-time polymerase chain reaction using SYBR green I depends on cDNA synthesis conditions`. *Anal. Biochem.* 307:63-69.

60. Wong ML & Medrano JF (2005) Real-time PCR for mRNA quantitation. *BioTechniques* 39:75-85.

61. Zhou L, Wang L, Palais R, Pryor R, & Wittwer C (2005) High-resolution DNA melting analysis for simultaneous mutation scanning and genotyping in solution. *Clin. Chem.* 51:1770-1777.

62. Sun Y & Fan X (2012) Distinguishing DNA by Analog-to-Digital-like Conversion by Using Optofluidic Lasers. *Angew. Chem. Int. Ed.* 51:1236 –1239.

63. Galas JC, Torres J, Belotti M, Kou Q, & Chen Y (2005) Microfluidic tunable dye laser with integratable mixer and ring resonator. *Appl. Phys. Lett.* 86:264101.

64. Tzeng H-M, Wall KF, Logng MB, & Chang RK (1984) Laser emission from individual droplets at wavelengths corresponding to morphology- dependent resonanaces. *Opt. Lett.* 9:499-501.

65. Kiraz A, *et al.* (2007) Lasing from single, stationary, dye-doped glycerol/water microdroplets located on a superhydrophobic surface. *Opt. Comm.* 276:145-148.

66. Jiang X, Song Q, Xu L, Fu J, & Tong L (2007) Microfiber knot dye laser based on the evanescent-wave-coupled gain. *Appl. Phys. Lett.* 90:233501.

67. Knight JC, Driver HST, Hutcheon RJ, & Robertson GN (1992) Core-resonance capillary-fiber whispering-gallery-mode laser. *Opt. Lett.* 17(18):1280-1282.

68. Moon H-J, Chough Y-T, & An K (2000) Cylindrical Microcavity Laser Based on the Evanescent-Wave-Coupled Gain. *Phys. Rev. Lett.* 85(15):3161-3164.
69. Sun Y, Suter JD, & Fan X (2009) Robust integrated optofluidic-ring-resonator dye lasers. *Opt. Lett.* 34(7):1042-1044.
70. Suter JD, *et al.* (2010) Demonstration of the coupling of optofluidic ring resonator lasers with liquid waveguides. *Opt. Lett.* 35(17):2997-2999.
71. Suter JD, Sun Y, Howard DJ, Viator JA, & Fan X (2008) PDMS embedded opto-fluidic microring resonator lasers. *Opt. Express* 16:10248-10253.
72. Shang L, Liu L, & Xu L (2008) Single-frequency coupled asymmetric microcavity laser. *Opt. Lett.* 33(10):1150-1152.
73. Wu X, Li H, Liu L, & Xu L (2008) Unidirectional single-frequency lasing from a ring-spiral coupled microcavity laser. *Appl. Phys. Lett.* 93:081105.
74. Chang-Yen DA, Eich RK, & Gale BK (2005) A Monolithic PDMS Waveguide System Fabricated Using Soft-Lithography Techniques. *JOURNAL OF LIGHTWAVE TECHNOLOGY* 23(6).
75. Xia Y, *et al.* (1997) Replica Molding Using Polymeric Materials: A Practical Step Toward Nanomanufacturing. *Advanced Materials* 9:147-149.
76. Xia Y & Whitesides GM (1998) Soft Lithography. *Angew. Chem. Int. Ed.* 37.
77. Abdolvand R & Ayazi F (2008) An advanced reactive ion etching process for very high aspect-ratio sub-micron wide trenches in silicon. *Sensors and Actuators A* 144:109-116.
78. Little BE, Laine J-P, & Haus HA (1999) Analytic Theory of Coupling from Tapered Fibers and Half-Blocks into Microsphere Resonators. *JOURNAL OF LIGHTWAVE TECHNOLOGY* 17(4).
79. Haus HA, Huang WP, Kawakami S, & Whitaker NA (1987) Coupled-Mode Theory of Optical Waveguides. *J. Lightwave Technol.* LT-5(1).
80. Ashkin A & Dziedzic JM (1977) Observation of resonances in the radiation pressure on dielectric sphere. *Phys. Rev. Lett.* 38:1351-1354.
81. Cai M, Painter O, & Vahala KJ (2000) Fiber-coupled microsphere laser. *Opt. Lett.* 25(19):1430-1432.

82. Chena G, Mazumdera MM, Changa RK, Swindalb JC, & Acker WP (1996) Laser diagnostics for droplet characterization: Application of morphology dependent resonances *Progress in Energy and Combustion Science* 22(2):163-188.
83. Lin H-B, Eversole JD, & Campillo AJ (1992) Spectral properties of lasing microdroplets. *J. Opt. Soc. Am. B* 9(1):43-50.
84. Sennaroglu A, A. Kiraz, Dündar MA, Kurt A, & Demirel AL (2007) Raman lasing near 630 nm from stationary glycerol-water microdroplets on a superhydrophobic surface. *Opt. Lett.* 32(15):1297-1299.
85. Hossein-Zadeh M & Vahala KJ (2006) Fiber-taper coupling to Whispering-Gallery modes of fluidic resonators embedded in a liquid medium. *Opt. Express* 14(22):10800-10810.
86. Tanyeri M, Perron R, & Kennedy IM (2007) Lasing droplets in a microfabricated channel. *Opt. Lett.* 32(17):2529-2531.
87. Tang SKY, *et al.* (2009) A multi-color fast-switching microfluidic droplet dye laser. *Lab Chip* 9(19):2767-2771.
88. Tang SKY, Derda R, Quan Q, Lončar M, & Whitesides GM (2011) Continuously tunable microdroplet-laser in a microfluidic channel. *Opt. Express* 19(3):2204-2215.
89. Groh W & Zimmermann A (1991) What Is the Lowest Refractive Index of an Organic Polymer? *Macromolecules* 24:6660-6663.
90. Polynkin P, Polynkin A, Peyghambarian N, & Mansuripur M (2005) Evanescent field-based optical fiber sensing device for measuring the refractive index of liquids in microfluidic channels. *Opt. Lett.* 30:1273-1275.
91. Teh S-Y, Lin R, Hung L-H, & Lee AP (2008) Droplet microfluidics. *Lab Chip* 8:198-220.
92. Chiu DT & Lorenz RM (2009) Chemistry and biology in femtoliter and picoliter volume droplets. *Acc. Chem. Res.* 42:649-658.
93. Sun Y, Shopova SI, Wu C-S, Arnold S, & Fan X (2010) Bioinspired optofluidic FRET lasers via DNA scaffolds. *Proc. Natl. Acad. Sci. USA* 107:16039-16042

94. Sun Y & Fan X (2011) Highly Selective Single-Nucleotide Polymorphism Detection with Optofluidic Ring Resonator Lasers. in *CLEO/QELS* (Baltimore, MD), p CWL6.

95. Sumetsky M, Dulashko Y, & Windeler RW (2010) Optical microbubble resonator. *Opt. Lett.* 35(7):898-890.

96. Sumetsky M, Dulashko Y, & Windeler RW (2010) Super free spectral range tunable optical microbubble resonator. *Opt. Lett.* 35(11):1866-1868.

97. Watkins A, Ward J, Wu Y, & Chormaic SN (2011) Single-input, spherical microbubble resonator. *Opt. Lett.* 36:2113-2115.

98. Stone J (1972) Measurements of the Absorption of Light in Low-Loss Liquids. *J. Opt. Soc. Am.* 62:327.

99. Fan X, Palinginis P, Lacey S, & Wang H (2000) Coupling semiconductor nanocrystals to a fused-silica microsphere: a quantum-dot microcavity with extremely high Q factors. *Opt. Lett.* 25(21):1600-1602.

100. Lacey S, *et al.* (2007) Versatile opto-fluidic ring resonator lasers with ultra-low threshold. *Opt. Express* 15:15523-15530.

101. Trivedi V, *et al.* (2010) A modular approach for the generation, storage, mixing, and detection of droplet libraries for high throughput screening. *Lab Chip* 10:2433-2442.

102. White IM, *et al.* (2007) Versatile waveguide-coupled opto-fluidic devices based on liquid core optical ring resonators. *Appl. Phys. Lett.* 91:241104.

103. Förster T (1959) Transfer mechanisms of electronic excitation. *Disc. Faraday Soc.* 27:7-17.

104. Shopova SI, *et al.* (2007) Opto-fluidic ring resonator lasers based on highly efficient resonant energy transfer. *Opt. Express* 15:12735-12742.

105. Shastry BS (2006) Pharmacogenetics and the concept of individual medicine. *Pharmacogenomics* 6:16-21.

106. Veer LJvt & Bernards R (2008) Enabling personalized cancer medicine through analysis of gene-expression patterns. *Nature* 452:564-570.

107. Bartlett JMS & Stirling D (2003) A Short History of the Polymerase Chain Reaction. *PCR Protocols* 226:3-6.

108. Li H & Rothberg LJ (2004) DNA Sequence Detection Using Selective Fluorescence Quenching of Tagged Oligonucleotide Probes by Gold Nanoparticles. *Anal. Chem.* 76:5414-5417.
109. Pohl G & Shih L-M (2004) Principle and applications of digital PCR. *Expert Rev. Mol. Diagn.* 4(1):41-47.
110. Shen F, Du W, Kreutz JE, Fok A, & Ismagilov RF (2010) Digital PCR on a SlipChip. *Lab Chip* 10:2666-2672.
111. Vogelstein B & Kinzler KW (1999) Digital PCR. *Proc. Natl. Acad. Sci. USA* 96:9236-9241.
112. Seipp MT, Durtschi JD, Voelkerding KV, & Wittwer CT (2009) Multiplex Amplicon Genotyping by High-Resolution Melting. *Journal of Biomolecular Techniques* 20:160-164.
113. SantaluciaJr. J (1998) A unified view of polymer, dumbbell, and oligonucleotide DNA nearest-neighbor thermodynamics. *Proc. Natl. Acad. Sci. USA* 95:1460–1465.
114. Siegman AE (1986) *Lasers* (University Science Books, Sausalito, CA).
115. Dimmick TE, Kakarantzas G, Birks TA, & Russell PSJ (1999) Carbon dioxide laser fabrication of fused-fiber couplers and tapers. *Appl. Opt.* 38:6845-6848.
116. Eklund EJ & Shkel AM (2007) Glass Blowing on a Wafer Level. *Journal of Microelectromechanical Systems* 16(2):232-239.
117. Grellier AJC, Zayer NK, & Pannell CN (1998) Heat transfer modelling in CO2 laser processing of optical fibres. *Opt. Commun.* 152:324-328.